J. Fluid Mech. (1994), *vol.* 259, *pp.* 345–373

On the role of the outer region in the turbulent-boundary-layer bursting process

By ROY Y. MYOSE† AND RON F. BLACKWELDER
Department of Aerospace Engineering, University of Southern California, Los Angeles, CA 90089-1191, USA

(Received 31 October 1991 and in revised form 26 July 1993)

The dynamics and interaction of turbulent-boundary-layer eddy structures was experimentally emulated. Counter-rotating streamwise vortices and low-speed streaks emulating turbulent-boundary-layer wall eddies were generated by a Görtler instability mechanism. Large-scale motions associated with the outer region of turbulent boundary layer were emulated with $-\omega_z$ spanwise vortical eddies shed by a periodic non-sinusoidal oscillation of an airfoil. The scales of the resulting eddy structures were comparable to a moderate-Reynolds-number turbulent boundary layer. Results show that the emulated wall-eddy breakdown was triggered by streamwise acceleration associated with the outer region of turbulent boundary layer. This breakdown involved violent mixing between low-speed fluid from the wall eddy and accelerated fluid associated with the outer structure. Although wall eddies can break down autonomously, the presence of and interaction with outer-region $-\omega_z$ eddies hastened their breakdown. Increasing the $-\omega_z$ eddy strength resulted in further hastening of the breakdown. Conversely, $+\omega_z$ eddies were found to delay wall-eddy breakdown locally, with further delays resulting from stronger $+\omega_z$ eddies. This suggests that the outer region of turbulent boundary layers plays a role in the bursting process.

1. Introduction

1.1. *Background*

Past studies (see Cantwell 1981) have shown that at least two types of organized structures exist in turbulent boundary layers. Near the wall are a series of small-scale low- (and high-) speed streamwise streaks. In the outer region, large-scale motions entrain non-turbulent fluid from outside the boundary layer. Cantwell (1981) classifies the near-wall region as $y^+ \leqslant 100$. (Viscous scaling denoted $()^+$ involves non-dimensionalization with the kinematic viscosity ν and the friction velocity defined by $u_\tau \equiv [\nu(\partial U/\partial y)|_{wall}]^{\frac{1}{2}}$.) The outer region is associated with the large-scale motions which scale with the boundary-layer thickness, δ. The ratio of these two scales is large and is proportional to the Reynolds number.

Klebanoff (1954) showed that 70–80 % of the turbulent energy production occurs in the near-wall region. In a phenomenon now known as the bursting process, Kline *et al.* (1967) found that the near-wall low-speed streaks lift up off the wall, oscillate, and then break down. Kim, Kline & Reynolds (1971) found that this bursting process was responsible for virtually all of the turbulent energy production near the wall. In experimental modelling studies, Acarlar & Smith (1987) and Swearingen & Blackwelder

† Present address: Department of Aerospace Engineering, Wichita State University, Wichita, KS 67260-0044, USA.

(1987) have found that the evolution and breakdown of streamwise vortices in laminar boundary layers were closely associated with the structure and dynamics of the bursting process.

Blackwelder & Kovasznay (1972) and Brown & Thomas (1977) showed that the outer-region large-scale motion was associated with $-\omega_z$ spanwise vortical motion. An important characteristic of the outer region is the upstream interface demarcating the turbulent and non-turbulent regions. Chen & Blackwelder (1978) found this interface to be quite distinct, stretching from the near-wall region ($y^+ < 35$) to the outer edge of the boundary layer. Both Brown & Thomas (1977) and Chen & Blackwelder observed an outward movement of fluid away from the wall as the interface approached and an insweep of high-speed fluid towards the wall after the passage of the interface.

In visual studies, Corino & Brodkey (1969), Smith (1978), Falco (1980) and Talmon, Kunen & Ooms (1986) found that the bursting process was followed by an insweep of high-speed fluid *thought* to emanate from the outer region. Blackwelder & Kaplan (1976) used a conditional-averaging (VITA detection) technique to study the bursting process quantitatively. They found an inflexional velocity profile associated with low-speed streaks prior to burst detection and a fuller velocity profile (caused possibly by the insweep of high-speed fluid) following detection. Using dynamical systems theory, Aubry *et al.* (1988) found that burst-like events could be generated autonomously in the wall region but the pressure fluctuations from the outer part of the boundary layer were the primary means of triggering the bursts. These studies therefore suggest an interactive relationship between the outer structure and the bursting process for low and moderate Reynolds numbers.

For a more extensive review of turbulent boundary layers, the reader is referred to Robinson (1991), Kline & Robinson (1989) and Cantwell (1981).

1.2. *Motivation and emulation method*

In a turbulent boundary layer, the near-wall eddies and outer-region structures appear randomly, both in time and in space. Since the exact phase relationship between these eddy structures is not known *a priori*, it is quite difficult to study the interaction between them. Thus it was resolved to emulate the eddy structures in a deterministic and periodic manner. The primary objective was to study the interaction of the eddy structures; that is, to study how the approach and passage of an ω_z vortex modelling the outer structure affects the streamwise vortices, low-speed streaks, etc., embedded in the near-wall region. In addition, the strength and sign of the outer spanwise eddy was varied to determine how such changes alter the interactive relationship.

The emulation technique is illustrated in figure 1. Counter-rotating streamwise vortices form and develop along the concave wall due to the Görtler instability mechanism. Only one pair of Görtler vortices is depicted although in reality many pairs exist with an average wavelength $\lambda \approx 2$ cm. Vortex shedding by an oscillating airfoil was used to generate large-scale ω_z spanwise eddies convecting periodically over the streamwise vortices. Although the experiment was not done in an *actual* turbulent boundary layer, it was an excellent emulation as discussed in §§1.3 and 4.2 suggesting that the results from this emulation experiment have direct relevance to turbulent boundary layers.

1.3. *Görtler vortical flow behaviour*

Görtler (1940) found that boundary-layer flow over a concave wall developed a primary instability in the form of a series of counter-rotating streamwise vortices. Bippes (1978), Aihara & Koyama (1981), Ito (1985), and Swearingen & Blackwelder (1987) found that low-speed streaks were formed as a result of the up-draught action

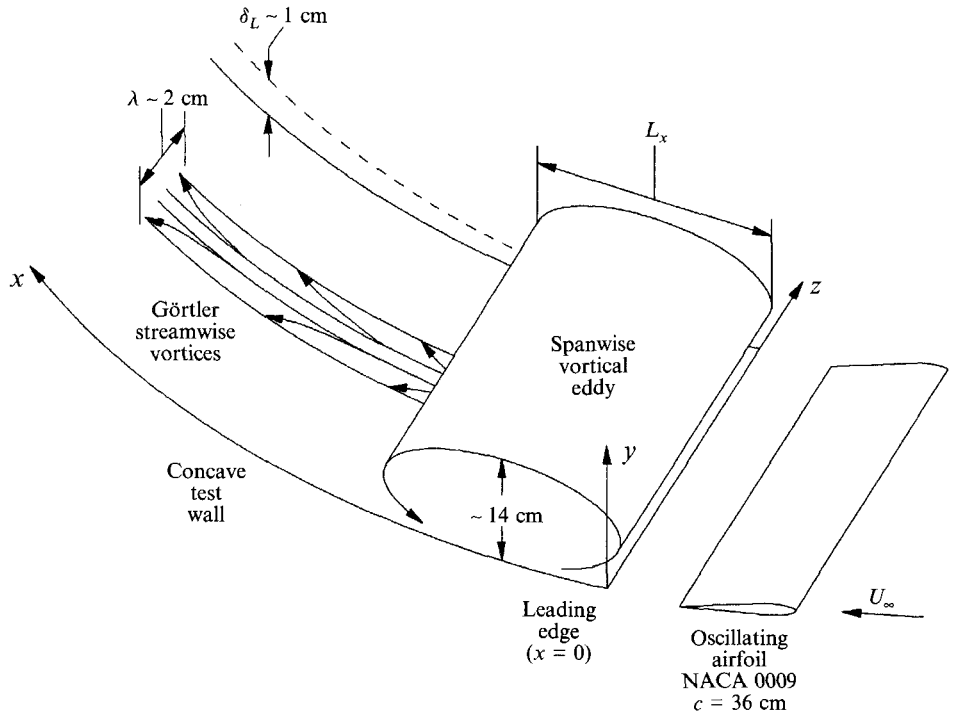

FIGURE 1. Emulation method and structures.

of counter-rotating streamwise vortex pairs. Strongly inflexional normal and spanwise velocity profiles were associated with the low-speed streaks. These inflexional profiles developed a secondary instability which appeared either in the form of horseshoe vortices or as a sinuous motion of the streamwise vortices. Swearingen & Blackwelder found that the sinuous motion associated with the spanwise shear $\partial u/\partial z$ was a major contributor to breakdown and transition to turbulence. According to Blackwelder (1983) and Swearingen & Blackwelder (1987), Görtler vortical flow behaviour is an excellent emulation of the near-wall behaviour in turbulent boundary layers. Both flows have streamwise vortices of about $50\nu/u_\tau$ height and develop low-speed streaks. The normal and spanwise velocity profiles are inflexional above and on the sides of the streaks in both flows. Both flow fields develop oscillations associated with the inflexional profiles and, finally, the breakdown process is similar. As with any analytical or experimental model, the correspondence between the emulation and the real flow will not be exact in every detail. For example, Guezennec, Piomelli & Kim (1989) and Robinson (1991) have pointed out that in turbulent flows the streamwise vortices rarely occur in pairs; however single streamwise vortices also produce low-speed streaks and it is the existence of the streaks and the associated inflexional profiles (and not necessarily their origin) that is important in the ensuing dynamics. In addition, the small scale of the wall layer, its randomness, etc., has hindered the study of this region and our knowledge of its dynamics is incomplete. Hence it was felt that an experimental study that modelled the primary dynamics of the wall region without the background turbulence could increase our understanding of that important region.

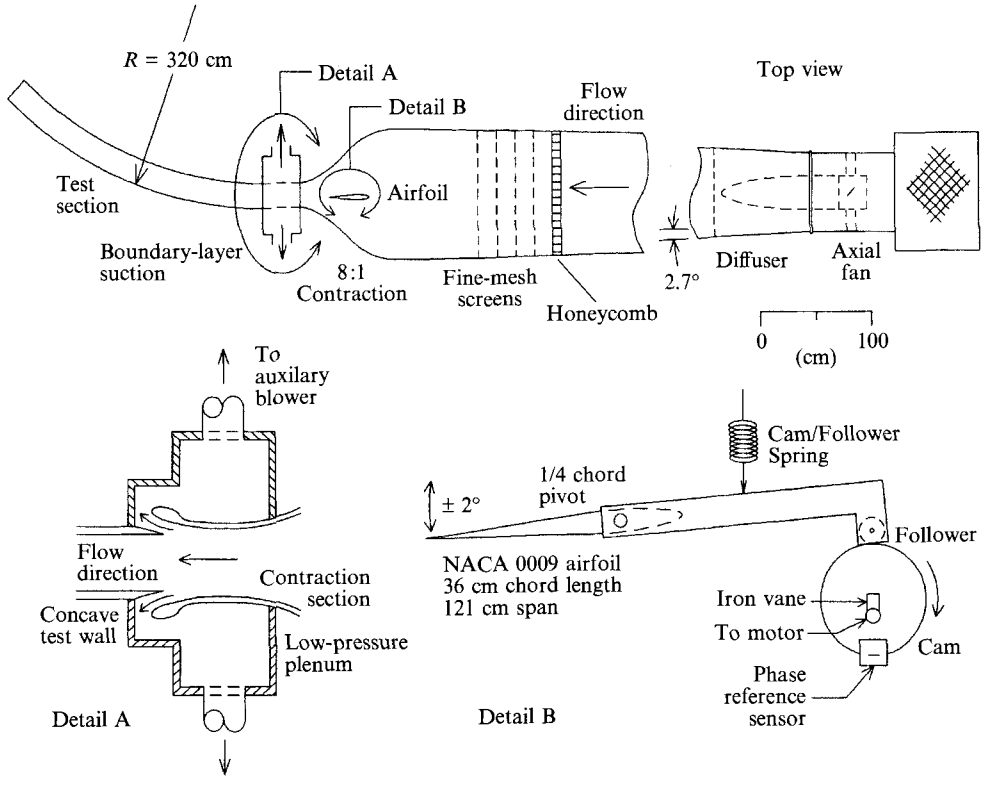

FIGURE 2. Schematic of experimental facility.

1.4. *Vortex shedding by an oscillating airfoil*

Vortex shedding by an airfoil in pitch oscillation is the consequence of circulation conservation according to Kelvin's theorem, i.e. $\mathrm{d}\Gamma(t)/\mathrm{d}t = 0$. When the pitch of an airfoil is changed, the circulation strength of the bound vortex over the airfoil changes. A vortex of strength equal and sign opposite to the *change* in the bound vortex is then shed off the airfoil in order to preserve Kelvin's circulation theorem. Thus, a $-\omega_z$ vortex is shed during airfoil pitch-down whereas a $+\omega_z$ vortex is shed during airfoil pitch-up according to the coordinate system shown in figure 1. When the airfoil is oscillated sinusoidally, $-\omega_z$ and $+\omega_z$ vortices of equal strength are shed during each oscillation cycle. Koochesfahani (1989) found that when the airfoil is oscillated non-sinusoidally, a concentrated vortex is shed during the rapidly pitching portion of the cycle whereas diffuse vortices are shed during the slower pitching portion of the cycle.

2. Experimental set-up

2.1. *Facility*

The experiments were conducted in the same low-turbulence facility used by Swearingen & Blackwelder (1987) which is shown schematically in figure 2. The test section is 245 cm long (in x) with a 15 cm (in y) by 120 cm (in z) cross-section and a 320 cm radius concave wall. Detail A of figure 2 shows the boundary-layer suction device which is used to tangentially remove the tunnel sidewall boundary layer so that the origin of the test-section boundary layer begins at the concave-wall leading edge. The oscillating airfoil was mounted with its pitch axis along the spanwise z-direction.

Detail B of figure 2 shows the airfoil oscillation mechanism which was driven by a computer-controlled stepping motor. For most cases, the off-centred circular cam was rotated at varying rates using a dedicated personal computer to generate customized pulse trains for the stepping motor. The addition of a (stationary) airfoil did not significantly alter the Görtler vortex flow behaviour (see Myose 1991). Thus, wall eddy development and breakdown without the outer spanwise eddies were reasonably comparable to those of Swearingen & Blackwelder (1987).

2.2. *Instrumentation and experimental apparatus*

Streamwise velocity measurements were made with constant-temperature hot-wire anemometers at 20% overheat. A ten-wire y-rake (with sensors at $y = 0.1$, 0.2, 0.3, 0.41, 0.61, 0.81, 1.12, 1.52, 1.93, and 2.54 cm) was used for interaction measurements. Airfoil phase referencing was accomplished with a Microswitch 4AV12C vane sensor. A thin strip of ferrous material was attached to the stepping-motor shaft which drove the cam (see detail B of figure 2). Whenever this ferrous vane passed through the gap of the sensor's magnet and transducer, a reference pulse signalled the start of a new airfoil oscillation cycle. In flow visualization experiments, the sensor signal was used to drive a LED which was visibly lit once an oscillation cycle.

The smoke-wire technique, described in detail by Swearingen (1985), was used for flow visualization. The 0.1 mm diameter stainless steel wire was located at $x = 22$ cm and $y = 0.14$ cm ($y/\delta_{\text{Blasius}} \approx 0.35$). The visualized flow pattern was recorded by a CCD camera and S-VHS video system. A time code generator imprinted a time reference every $\frac{1}{30}$th of a second on the video; however, the video recording speed was $\frac{1}{60}$th of a second.

3. Experimental procedure

In all experiments, the free-stream velocity was maintained at $U_\infty = 500$ cm s$^{-1} \pm 1$% using a pressure transducer and Pitot tube located at $x = 10$ cm.

3.1. *Hot-wire measurements*

Before the start of an experimental run, the standard frequency response adjustment and hot-wire calibration was performed. Figure 3 shows the schematic diagram of the experimental procedure. For each measurement, the airfoil was oscillated for about 3 s before data acquisition was started to eliminate any transients. The hot-wire and airfoil phase-reference signals were simultaneously acquired by the analog-to-digital converter, typically at a 2 KHz sampling rate. All measurements consisted of about 100 oscillation cycles. For spanwise vortical eddy measurements, a single-sensor hot-wire probe was traversed in the vertical y-direction at 1 cm intervals. For interaction measurements, the y-rake was traversed over a range of spanwise z-locations at 0.1 cm intervals. At the conclusion of each measurement, the airfoil oscillation was stopped and the drift from the calibration curve of each hot wire was checked. Almost all of the measurements involved hot-wire drifts of less than 1%. Any data with a drift greater than 2% were rejected.

3.2. *Averaging technique*

In this experiment, the cyclic oscillation of the airfoil produces a periodic flow field. Thus, the velocity $u(\boldsymbol{x}, t)$ can be decomposed into three parts (see Jayaraman, Parikh & Reynolds 1982):

$$u(\boldsymbol{x}, t) = \bar{u}(\boldsymbol{x}) + \tilde{u}(\boldsymbol{x}, t) + u'(\boldsymbol{x}, t),$$

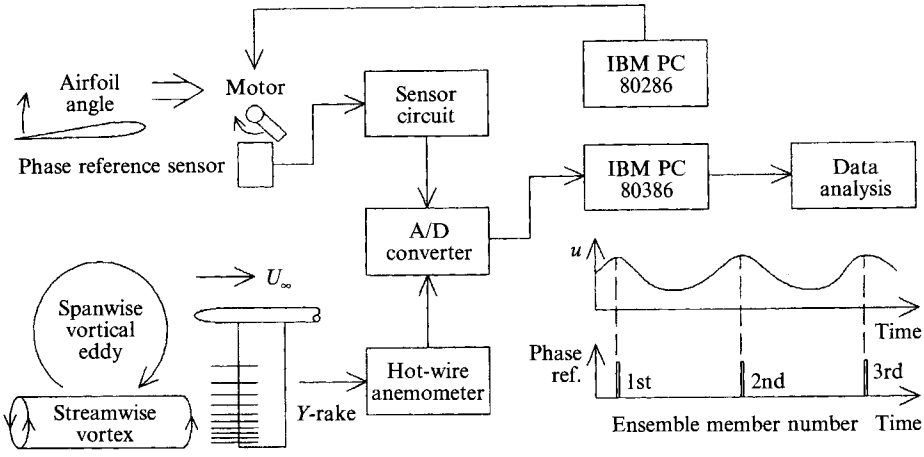

FIGURE 3. Block diagram of experimental procedure.

where $\bar{u}(x)$ is the time-averaged, $\tilde{u}(x,t)$ the periodic and $u'(x,t)$ the random fluctuating parts of the velocity. The ensemble-averaged velocity $\langle U(x,\phi)\rangle$ is defined as

$$\langle U(x,\phi)\rangle = \bar{u}(x)+\tilde{u}(x,\phi) = \sum_{n=1}^{N} u(x,n\phi)/N \quad \text{for} \quad 0 \leqslant \phi \leqslant 2\pi,$$

where N is the number of ensemble members (i.e. number of cycles) and ϕ is the phase. The standard deviation from the ensemble average $u'_{sd}(x,\phi)$ is given by

$$u'_{sd}(x,\phi) = (\langle u'(x,\phi)^2\rangle)^{\frac{1}{2}},$$

which provides a measure of the random component of the velocity. For brevity, the functional dependence of $\langle U\rangle$ and u'_{sd} will not be explicitly expressed; it will be understood that they are functions of phase ϕ and position $x(x,y,z)$. To facilitate data comparison, the zero reference time, $\phi = 0$, at each downstream x-location was defined as the time of the $-\omega_z$ eddy arrival. The measured convection velocity of the spanwise vortical eddy was 500 cm s^{-1}. Thus, its arrival time downstream was easily calculated.

4. Spanwise vortical eddies

In all experiments, the airfoil was oscillated over $\pm 2°$ at a frequency of 5 Hz$\pm$ 0.1%. This resulted in a reduced frequency of 1.4. (The reduced frequency K is defined as $K = \pi fc/U_\infty$ where f is the oscillation frequency and c is the airfoil chord length.) The chord Reynolds number of the airfoil was about 10^5. Throughout this paper, the percentage of time spent in the pitch-down mode is used to differentiate the various non-sinusoidal oscillation cases; e.g. the 35% oscillation case refers to an airfoil pitch-down time of $0.35T$ (where T = period) followed by pitch-up for $0.65T$.

4.1. *Results*

Figure 4 shows the ensemble-averaged streamwise velocity as a function of phase at six different heights for the 35% oscillation case. During the first 35% of the phase cycle, the velocity $\langle U\rangle$ is less than average in the lower half of the test-section channel width ($y < 7.5$ cm) while it is greater than average in the upper half ($y > 7.5$ cm), consistent with the presence of strong $-\omega_z$ vorticity (i.e. $+\partial u/\partial y$). A strong acceleration is apparent between 0.35π and 0.7π. The acceleration was also evident upstream (not

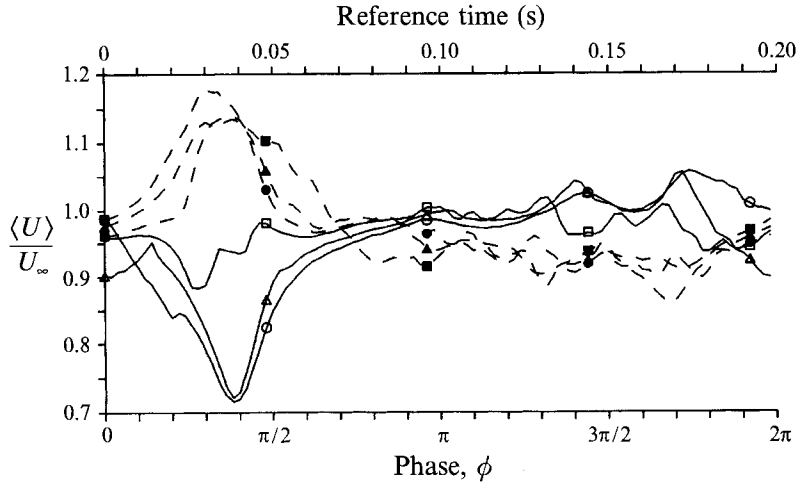

FIGURE 4. Trace of ensemble-averaged velocity $\langle U \rangle / U_\infty$ for the 35% oscillation case at $x = 82.5$ cm, $z = 10$ cm. —○—○—, $y = 2.5$ cm; —△—△—, $y = 4.5$ cm; —□—□—, $y = 6.5$ cm; -●-●-, $y = 8.5$ cm; -▲-▲-, $y = 10.5$ cm; -■-■-, $y = 12.5$ cm.

shown) before breakdown occurred; hence it is associated with the outer eddy structure and not with the breakdown itself. During the later 65% of the phase cycle, weaker and diffuse $+\omega_z$ vorticity is apparent. The instantaneous fluctuating velocity $u'(t)$ as well as some limited flow visualization showed that the spanwise vortical eddies were turbulent, with $u'_{sd}/U_\infty \approx 0.05$. This was not surprising since the chord Reynolds number was transitional.

The spanwise vortical eddies were two-dimensional according to hot-wire results from several spanwise z-locations as well as some limited flow visualization. Therefore, the two-dimensional continuity equation was used to compute the vertical velocity $\langle V \rangle$. The streamline patterns were computed from lines of constant stream function Ψ given by

$$\Psi = \int U \, dy - \int \langle V \rangle \, dx,$$

where $U \equiv \langle U \rangle - U_c$ for a convected frame of reference. The streamline flow patterns (i.e. constant stream function Ψ) in a convected frame of reference (with $U_c = 500$ cm s^{-1}) for the 25%, 35%, 50% and 65% oscillation cases are shown in figure 5 at a downstream location of $x = 82.5$ cm. Strictly speaking, an increase in the stream-function contour level does not represent an increase in vorticity. However, when the stream-function contours are close together, the vortex is concentrated; that is, the same net amount of circulation strength is compacted into a spatially smaller area, resulting in a stronger vortex. Consequently, tightly compacted closed streamline patterns in figure 5 can be interpreted as a strong ω_z vortex and, conversely, diffuse patterns as a weak ω_z vortex.

The four different oscillation cases shown in figure 5 were arranged so that the airfoil pitch-down time progressively increased from top to bottom. It is apparent from the figure that the generated $-\omega_z$ vortex/vortices were progressively weaker as the pitch-down time was lengthened. Furthermore, in the 65% case a series of $-\omega_z$ vortices were shed rather than a single $-\omega_z$ vortex. This was consistent with the envisioned generation mechanism where diffuse vortices are shed during the slower-pitching portion of the cycle. Also consistent were the phase reference times demarcating the

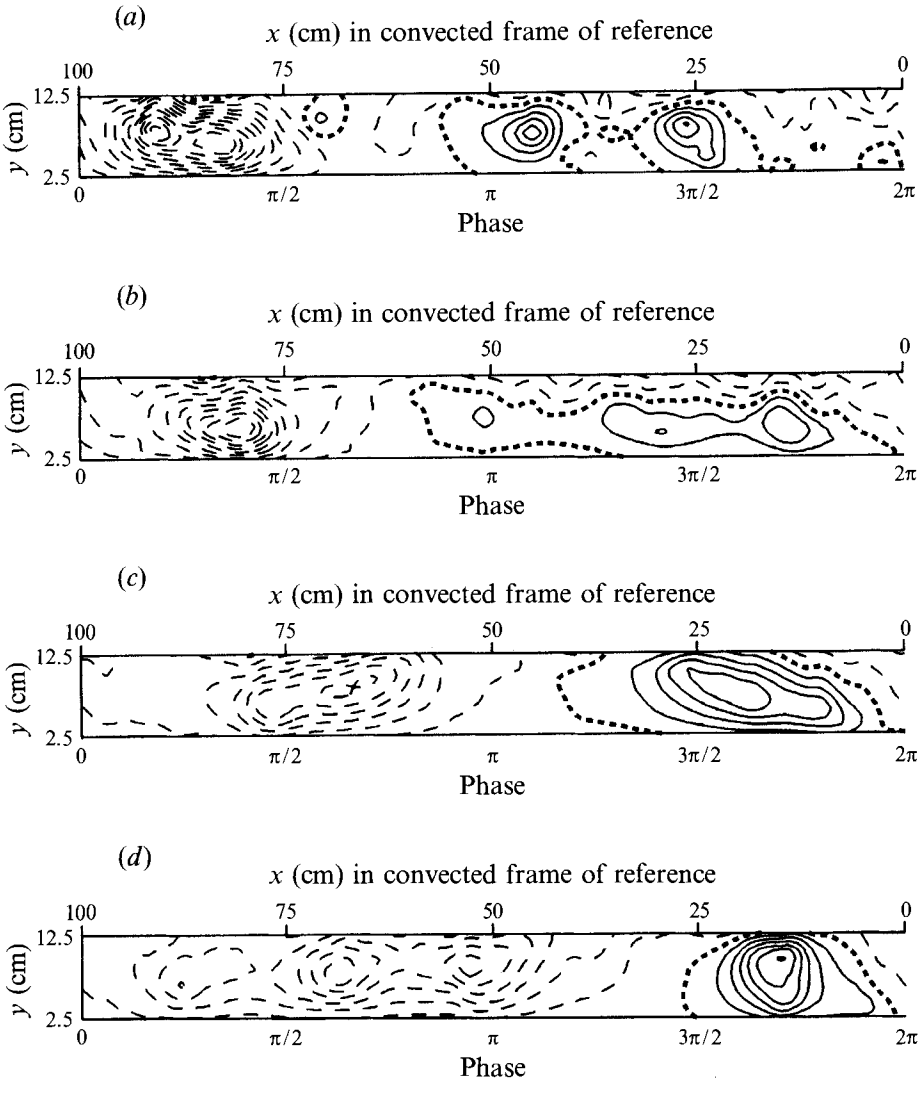

FIGURE 5. Lines of constant stream function Ψ for different oscillation cases. – – $\Psi < 0$ ($-\omega_z$ vortex); —— $\Psi > 0$ ($-\omega_z$ vortex); – – $\Psi = 0$; contour levels are 100 cm^2 s^{-1} apart. (*a*) 25% oscillation case at $x = 82.5$ cm, $z = 10$ cm. (*b*) 35% case at $x = 82.5$ cm, $z = 10$ cm. (*c*) 50% case at $x = 82.5$ cm, $z = 10$ cm. (*d*) 65% case at $x = 82.5$ cm, $z = 10$ cm.

$-\omega_z$ and $+\omega_z$ vortices according to the pitch-down and pitch-up times. For example, the $-\omega_z$ eddy passage was during $0 \leqslant \phi \leqslant 0.7\pi$ with the vortex centre at about $\phi \approx 0.35\pi$ to 0.4π for the 35% oscillation case (see figure 5*b*). Figure 5 also shows that $+\omega_z$ vortices generally became stronger as the pitch-up time was reduced. (Two relatively strong $+\omega_z$ vortices were generated in the 25% case; the exact reason for this is not known at this time.) Results at other x-locations showed that there was a small amount of dissipation of the vortices with downstream distance. When normalized with the calculated Blasius velocity gradient at the wall, the ensemble-averaged vorticity peaks at $x = 82.5$ cm were -0.19, -0.15, -0.062 and -0.067 for the 25%, 35%, 50% and 65% oscillation cases respectively. The corresponding maximum $+\omega_z$ peaks were $+0.19$, $+0.062$, $+0.086$ and $+0.11$.

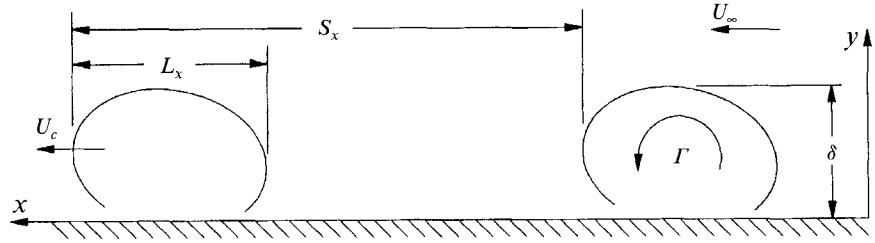

FIGURE 6. Sizing comparison of emulated outer-region structure and turbulent boundary layer (TBL).
Height $\delta \approx 14$ cm ($\Rightarrow \mathrm{Re}_\theta \approx 5200$)
Streamwise length $L_x \approx 2.5\delta$ ($\delta \leqslant L_x \leqslant 3\delta$ for TBL)
Streamwise spacing $S_x \approx 7\delta$ ($2\delta \leqslant S_x \leqslant 9\delta$ for TBL)
Convection velocity $U_c \approx U_\infty$ ($0.8U_\infty \leqslant U_c \leqslant 0.9U_\infty$ for TBL)
Strength $\Gamma \sim 0.4\delta U_\infty$ ($\Gamma \sim \delta U_\infty$ for TBL).

4.2. *Spanwise vortical-eddy sizing comparison*

In this section, $-\omega_z$ vortical eddies generated by the 35% oscillation case are compared to those in actual turbulent boundary layers. The outer-region structures of actual turbulent boundary layers are three-dimensional with a finite spanwise width (Cantwell 1981). However, no evidence exists suggesting that the three-dimensionality is important in the interaction, and thus to simplify the study, the emulated structures were two-dimensional and spanned the entire test section. The issue of interaction with three-dimensional outer-region structure is briefly addressed by Myose (1991).

Figure 6 defines the various quantities associated with the outer-region structure of turbulent boundary layers. The figure also lists the comparative sizes of the emulated ($35\% - \omega_z$) structure and actual turbulent boundary layers. The height of the actual outer-region structure is equal to the boundary-layer thickness δ and continues down into the near-wall region, if not to the wall itself. Cantwell (1981) gives a streamwise length in the range $\delta \leqslant L_x \leqslant 2\delta$ although Blackwelder & Kovasznay (1972) measured a value of $L_x \approx 3\delta$. Based on values given by Cantwell, the streamwise spacing between successive outer-region structures is in the range $2\delta \leqslant S_x \leqslant 9\delta$. The convection velocity is in the range $0.8U_\infty \leqslant U_c \leqslant 0.9U_\infty$.

A value for the circulation strength of the outer eddies in a turbulent-boundary-layer flow was not available in the literature so an estimate was made instead. Circulation strength is given by the relationship

$$\Gamma = \int\int \left[\frac{\partial v}{\partial x} - \frac{\partial u}{\partial y}\right] \mathrm{d}x\,\mathrm{d}y.$$

The streamwise velocity was assumed to follow a $\frac{1}{7}$th power law and contributions from the v-velocity were neglected. The range of integration over the eddy was 0 to L_x in the x-direction and was from the lower end of the logarithmic region ($y^+ \approx 35$) to the edge of the boundary layer ($y = \delta$) in the y-direction. Using a friction velocity of $u_\tau = 0.03U_\infty$, the circulation strength is found to be

$$\Gamma = L_x U_\infty \{[35\nu/(0.03U_\infty \delta)]^{\frac{1}{7}} - 1\}.$$

For $L_x \approx 3\delta$, $U_\infty = 500$ cm s^{-1} and $\delta = 14$ cm, $\Gamma \approx -8600$ cm^2 s^{-1} $\approx -1.2\delta U_\infty$. Hence, the outer turbulent eddy has a circulation of roughly δU_∞ with a $-z$ rotation.

Turning to the emulated structure, the circulation strength of the shed vortex is proportional to the change in airfoil lift, i.e.

$$\Gamma = \tfrac{1}{2} U_a c \Delta c_l,$$

where U_a is the velocity over the airfoil, c is the chord length and Δc_l is the change in lift coefficient. The average velocity over the airfoil in the contraction section was $U_a \sim 350$ cm s^{-1}. For an airfoil oscillation of $\pm 2°$ (or $\Delta\alpha = 4°$) and a NACA 0009 airfoil lift curve slope of 0.104 deg.$^{-1}$, the change in lift coefficient was $\Delta c_l \approx 0.42$. With a chord length of 36 cm, an analytical estimate of the circulation strength was $\Gamma \approx 2650$ cm^2 s^{-1}.

The vertical extent of the $-\omega_z$ vortical eddy encompassed the entire test-section channel width (of 15 cm) less the convex-section boundary layer. Thus, the vertical height of the spanwise vortical eddy, that is the emulated δ, was taken to be 14 cm. The streamwise length of the $-\omega_z$ vortex was 35 cm ($0.35TU_c$) and the streamwise spacing was 100 cm (TU_c) which gives $L_x \approx 2.5\delta$ and $S_x \approx 7\delta$. The convection velocity was $U_c \approx 500$ cm s$^{-1} = U_\infty$, and the circulation strength was given above to be $\Gamma \approx 2650$ cm^2 s$^{-1} \approx 0.4\delta U_\infty$. These parameters yield $Re_\theta \approx 5200$ for the emulated turbulent boundary layer. Figure 6 shows that all of the emulation sizes compare favourably with the actual turbulent boundary layer.

One possible difference between the actual and emulated structures may be the phase of the high-speed insweep and acceleration. In actual turbulent boundary layers, an acceleration due to an insweep of high-speed fluid is *thought* to appear after the passage of the outer-region structure (i.e. at the rear interface). (In actual turbulent boundary layers, the insweep also involves fluid motion towards the wall ($-\Delta v$). Owing to the particular way the oscillating airfoil mechanism produced $-\omega_z$ vortical eddies, it was not possible to generate a strong $-\Delta v$ along with the streamwise acceleration.) In the emulated structure, figure 4 shows that acceleration at the lower heights starts from the middle of $-\omega_z$ eddy passage, i.e. from $\phi \approx 0.35\pi$ to 0.4π and is an integral part of the $-\omega_z$ spanwise eddy. Hence the acceleration in the wall region is a consequence of and directly associated with the outer region structure. Another difference is that no isolated pockets of high-speed fluid reported by Falco (1980) were observed in the present study. In spite of these differences, the generated structures provide a good test bed to study the breakdown of streamwise vortices due to the disturbance of a large spanwise vortex passing over them. Thus they are a good emulation of the interactive relationship between turbulent-boundary-layer eddy structures.

5. Interaction of eddy structures emulating turbulent boundary layers (35% case)

Throughout this paper, the term 'wall eddy' is used in reference to the organized structures of the near-wall region. Wall eddies are characterised by streamwise vortices, low- and high-speed regions, strong normal and spanwise shear, and organized wall shear structure. These characteristics appear to set up an inflexional instability and oscillations which cease to exist in the wall region when *breakdown* occurs.

5.1. *Flow visualization results*

Figure 7 shows a typical smoke-wire flow visualization for the 35% oscillation case. Note that the photographic reproduction was mirror-imaged so that the x-distance labels of 60–100 cm at midspan ($z = 0$ cm) are reversed. The vertical and horizontal grid lines are 10 cm apart. The phase is shown at the top of the figure in radians. The arrival of the accelerated region (beginning at $\phi \approx 0.35\pi$ to 0.4π) is indicated at the bottom of the figure.

Figure 7 shows that small oscillations of the low-speed streaks marked by smoke precede the arrival of the acceleration region (e.g. at $\phi \approx 0$, $x \approx 100$ cm). A large

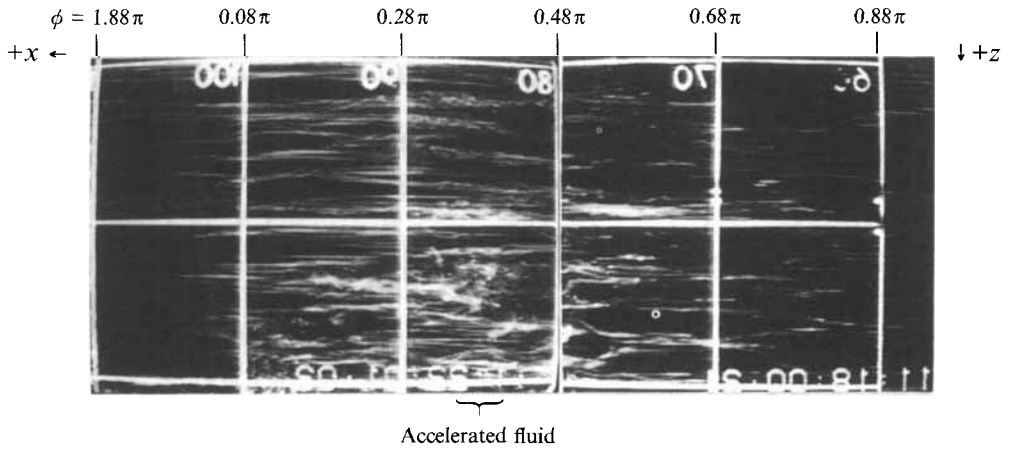

FIGURE 7. Flow visualization for 35% oscillation case. A composite of two video frames (with the break at $x = 80$ cm) which were taken at a comparably similar instant in time.

mixing of smoke particles in the wall region (e.g. at $\phi \approx 0.4\pi$, $x \approx 85$ cm) indicated by the white smoke puffs accompanies the accelerated region. In §5.2, it will be shown that this mixing corresponds to random motions in the wall region along with a breakdown of the low-speed streak structure. Thus, the breakdown is associated with the arrival of the accelerated region. Upstream of the accelerated region (e.g. at $\phi \approx 0.7\pi$, $x \approx 70$ cm), the undisturbed flow state begins to return in the wall region. Thus, the interaction involves a cyclic process consisting of: (i) $-\omega_z$ eddy arrival and low-speed streak oscillation; (ii) the triggering of breakdown of wall eddy structure along with tremendous mixing and random motions; followed by (iii) a return to the undisturbed flow state. Additional flow visualization (see Myose 1991) showed that the broken down region of mixed fluid grew downstream to encompass a larger portion of the phase cycle until the entire flow was turbulent at $x \sim 125$ cm.

5.2. *Quantitative results*

Figure 8 shows the instantaneous fluctuation signal u'/U_∞ (i.e. $\langle U \rangle$ has been removed) for all ten hot wires centred spanwise over a low-speed streak at $x = 82.5$ cm. (The spanwise location of the low-speed streak is stable and well established in the Görtler flow system.) Five oscillation cycles ($0 \leqslant \phi \leqslant 5 \times 2\pi$) are shown and the velocity scale is given on the left. A prominent feature of the instantaneous signal was the similarity in the flow response from one cycle to the next. Note that the relatively small-amplitude high-frequency fluctuations far from the wall ($y^+ > 100$) are associated with the outer-region ω_z structure. Figure 8 shows high-frequency fluctuations in the near-wall region ($y^+ < 100$) starting from $\phi \approx 0.4\pi + 2\pi n$ (where n corresponds to the cycle number) and lasting until $\phi \approx \pi + 2\pi n$. Note that the high-frequency velocity fluctuations correspond to the visual observations of mixing of the smoke particles seen in figure 7. Often, there were high-amplitude low-frequency fluctuations between the high-speed fluid regions (e.g. $\phi \approx 4\pi$ and $\phi \approx 8\pi$ in figure 8). By comparison with the flow visualization during comparable phase times (e.g. figure 7), these low-frequency velocity fluctuations seem to be associated with meandering of the low-speed streaks similar to that seen in the early stages of the turbulent-boundary-layer bursting process.

Figure 8 shows that the general characteristics of the flow at any given height within the near-wall region are quite similar. Thus, a single height of $y = 0.3$ cm was chosen

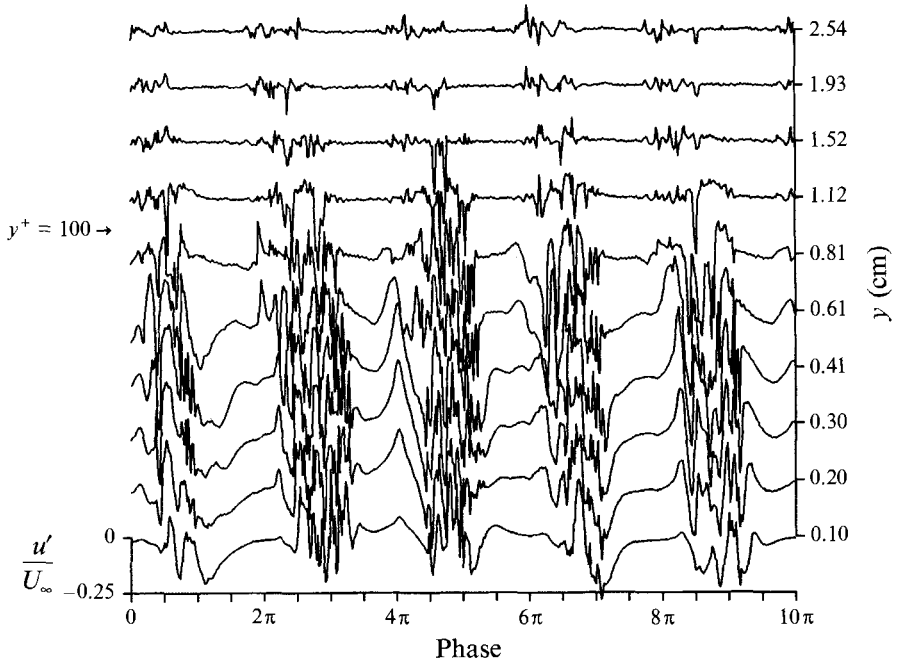

FIGURE 8. Instantaneous signal u'/U_∞ at $x = 82.5$ cm, $z = 9.5$ cm for the 35% oscillation case.

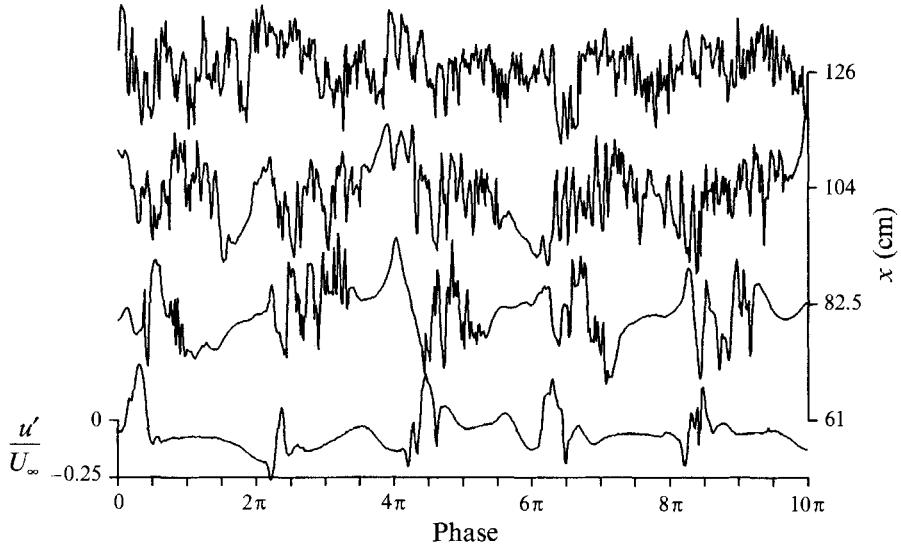

FIGURE 9. Instantaneous signal u'/U_∞ at various downstream locations for the 35% oscillation case. Signal shown is at $y = 0.3$ cm and centred spanwise over a low-speed streak.

to explore the downstream development of the breakdown of the u'/U_∞ signals shown in figure 9. At $x = 61$ cm, the flow response typically involved moderately low-frequency fluctuations centred at $\phi \approx 0.4\pi + 2\pi n$. Small oscillations (but not mixing of smoke particles) were observed during comparable phase times at $x = 60$ cm in flow visualization. At this downstream location, the wall eddies were not broken down and the oscillations appeared to be due to meandering of the low-speed streaks. At

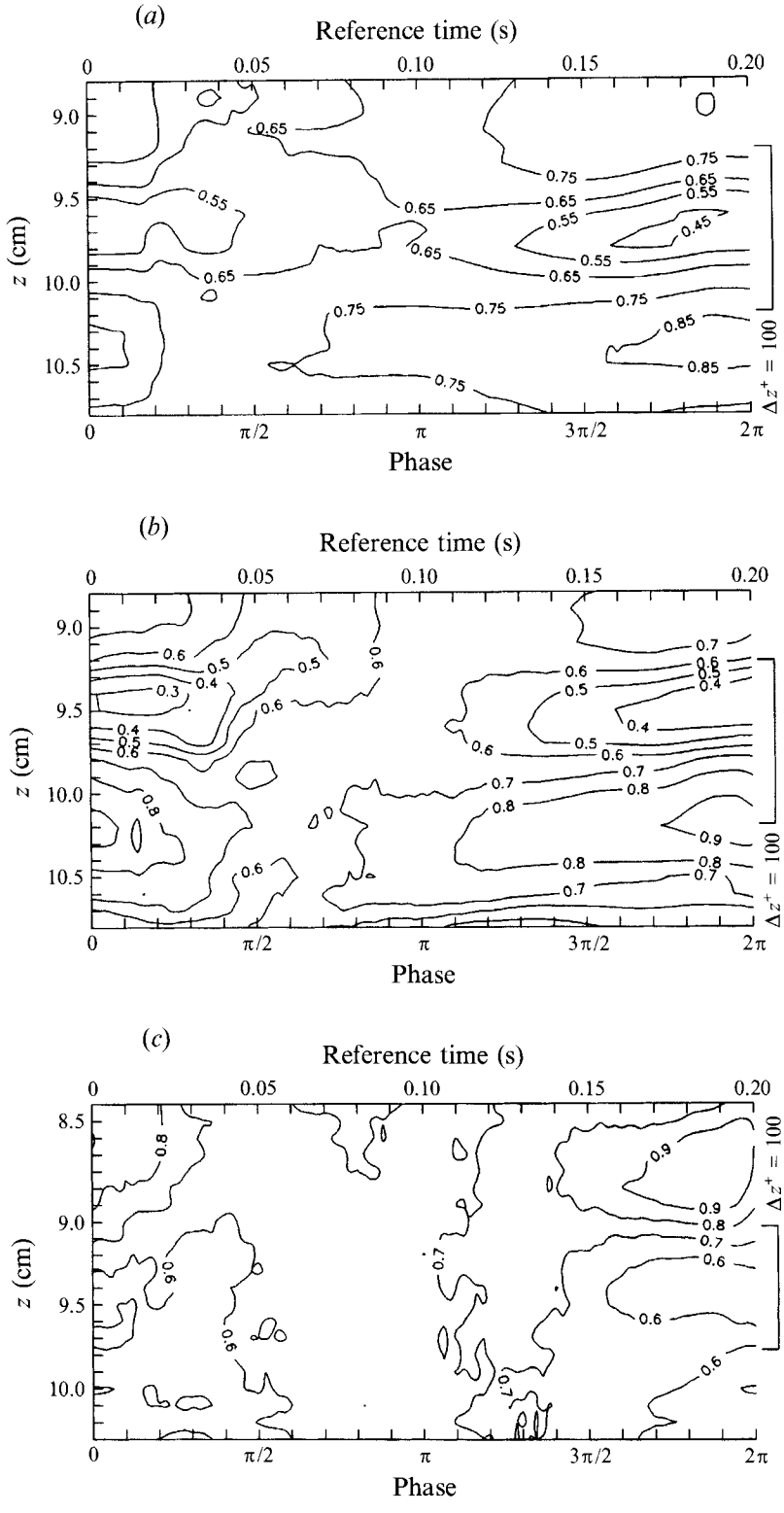

FIGURE 10. Iso-contours of $\langle U \rangle / U_\infty$ for the 35% oscillation case at $y = 0.3$ cm. $\langle U \rangle$ contours are $0.1 U_\infty$ apart. (*a*) $x = 61$ cm ($y^+ = 31$); (*b*) $x = 82.5$ cm ($y^+ = 34$); (*c*) $x = 104$ cm ($y^+ = 40$).

$x = 82.5$ cm, a sizeable fraction of each phase cycle involved the high-frequency fluctuations that signify wall-eddy breakdown. Further downstream, at $x = 104$ cm, a larger fraction of each phase cycle was broken down as indicated by the high-frequency fluctuations. There were only small cyclic intervals of quiescence. Finally at $x = 126$ cm, the entire flow in the near-wall region was broken down with high-frequency fluctuations.

The downstream development of the breakdown is further illustrated in figure 10 by the averaged $\langle U \rangle / U_\infty$ iso-contour plots. Since the phase increases from left to right, the pseudo-x direction in a convected frame of reference increases from right to left consistent with the flow visualization photograph of figure 7. Thus, the figure shows iso-contours in the x, z cross-section at a height of $y = 0.3$ cm. At $x = 61$ cm in figure 10(*a*), a low-speed streak is centred at about $z \approx 9.7$ cm and high-speed streaks are found at $z \approx 9.0$ cm and $z \approx 10.4$ cm. During the later part of the phase cycle (i.e. $1.3\pi \lesssim \phi \leqslant 2\pi$) and the early part preceding the arrival of the acceleration (i.e. $0 \leqslant \phi \lesssim 0.4\pi$), the spanwise velocity difference between the low- and high-speed streaks is quite pronounced ($\Delta U \approx 0.2 U_\infty$ to $0.4 U_\infty$). With the arrival of the accelerated fluid ($\phi \geqslant 0.4\pi$), the velocity difference between the low- and high-speed streaks is much smaller. Nevertheless, the persistent existence of a low-speed streak structure is apparent from the figure and the wall-eddy structure is not yet broken down at $x = 61$ cm. This conclusion is also supported by the flow visualization of Myose (1991) and the lack of high-frequency fluctuations in the instantaneous u' signal in figure 9 at this downstream location.

At $x = 82.5$ cm, in figure 10(*b*), there is a low-speed streak centred at about $z \approx 9.5$ cm and high-speed streaks at $z \approx 8.8$ cm and $z \approx 10.2$ cm. The low- and high-speed streak structure is less coherent at $0.4\pi \leqslant \phi \lesssim 1.1\pi$ following the arrival of the accelerated fluid. During this time frame, there was tremendous mixing in the flow visualization in figure 7 and high-frequency fluctuations occur in the instantaneous u' signal in figure 9. Thus the breakdown is associated with (and may be instigated by) the arrival of the acceleration.

Further downstream at $x = 104$ cm, figure 10(*c*) shows breakdown of the low-speed streak structure over $0.1\pi \lesssim \phi \lesssim 1.5\pi$. The low-speed streak structure is present only during $1.5\pi \lesssim \phi \lesssim 2.1\pi$ which is consistent with flow visualization of Myose (1991) and the instantaneous u' signal in figure 9. In this convected frame, the leading edge of breakdown has moved forward to about $\phi \approx 0.1\pi$ which temporally precedes the arrival of accelerated fluid at this downstream location. Additional results show an absence of low-speed streak structure by $x = 126$ cm which is consistent with the presence of high-frequency fluctuations over the entire phase cycle in figure 9.

Figure 11 shows additional iso-contours of the ensemble-averaged quantities at $x = 82.5$ cm. The results are better understood by classifying them under two different events. The first event, for $1.1\pi \lesssim \phi \leqslant 2\pi$ and $0 \leqslant \phi \leqslant 0.4\pi$, is the pre-breakdown oscillation phase, and the second event, for $0.4\pi \leqslant \phi \lesssim 1.1\pi$, is the breakdown phase. During the pre-breakdown oscillation phase, there was meandering of the low-speed streak in flow visualization seen in figure 7 and low-frequency fluctuations in the instantaneous u' signal seen in figure 8. Figure 11(*a*) shows that relatively large fluctuations (e.g. $0.08 \leqslant u'_{sd}/U_\infty \leqslant 0.12$) are associated with this low-speed streak oscillation. Figure 11(*b*) shows large-magnitude spanwise shear (i.e. $[\partial \langle U \rangle / \partial z]/[\partial U/\partial y|_{w,a}]$ less than -0.2 and greater than 0.2) during this pre-breakdown oscillation phase. A comparison between spanwise shear in figure 11(*b*) and ensemble-averaged velocity in figure 10(*b*) shows that large-magnitude spanwise shear occurs on the spanwise sides of the low-speed streak. Furthermore, a comparison of figures 11(*a*)

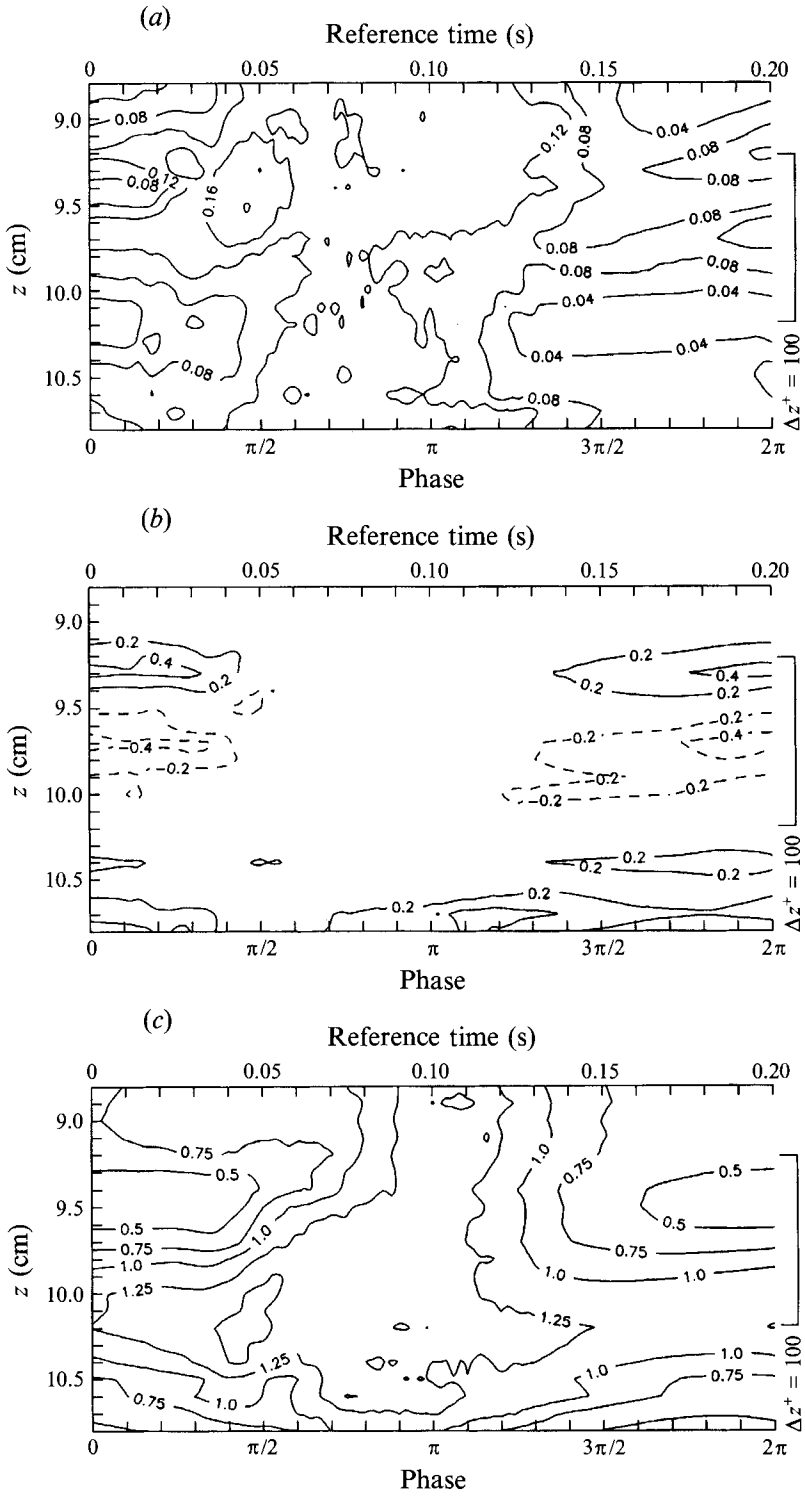

FIGURE 11. Iso-contours for the 35% oscillation case at $x = 82.5$ cm. (*a*) u'_{sd}/U_∞ at $y = 0.3$ cm ($y^+ = 34$); (*b*) $[\partial\langle U\rangle/\partial z]/[\partial U/\partial y|_{w,a}]$ at $y = 0.3$ cm ($y^+ = 34$), ---, contours < 0; (*c*) wall shear, $[\partial\langle U\rangle/\partial y|_{y=0}]/[\partial U/\partial y|_{w,a}]$. Computed shear was normalized by the average wall shear of $\partial U/\partial y|_{w,a} = 1910\ \text{s}^{-1}$.

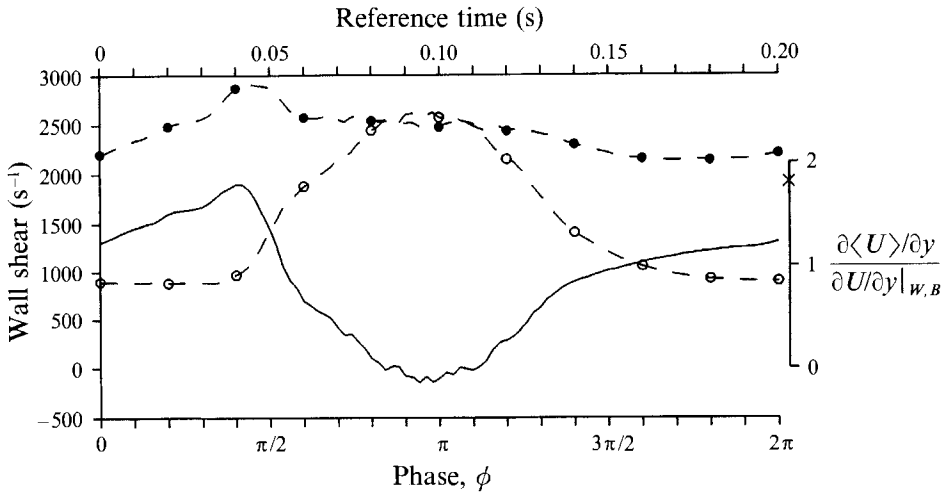

FIGURE 12. Wall shear, $\partial\langle U\rangle/\partial y|_{wall}$, for the 35% oscillation case at $x = 82.5$ cm. –●–●–, $\partial\langle U\rangle/\partial y|_{w,h}$, wall shear at high-speed region; –○–○–, $\partial\langle U\rangle/\partial y|_{w,l}$, wall shear at low-speed region; ——, $\partial\langle U\rangle/\partial y|_{w,h} - \partial\langle U\rangle/\partial y|_{w,l}$, difference between high- and low-speed streak wall shears; ×, time-averaged wall shear (over both low- and high-speed regions). The scale on the right is normalized with the wall shear for a Blasius boundary layer, $\partial U/\partial y|_{w,B}$.

and 11(*b*) shows that spanwise shear is correlated with the large fluctuations. Swearingen & Blackwelder (1987) found relatively large fluctuations and spanwise shear on the sides of the low-speed streak during the later stages of Görtler flow development preceding breakdown to turbulence.

During the second event, a breakdown of the wall-eddy structure occurs associated with the arrival of the accelerated fluid. This results in high-frequency random motions indicated by very high levels of u'_{sd} at *all* spanwise locations in figure 11(*a*). The maximum fluctuation level of $u'_{sd}/U_\infty > 0.16$ occurs at a spanwise location centred about the low-speed streak (i.e. at $z \approx 9.5$ cm) and at a phase $\phi \approx 0.4\pi$ correlated with the arrival of accelerated fluid. Figure 11(*b*) shows an absence of spanwise shear during breakdown since the low-speed streak structure is destroyed and a velocity deficit in the spanwise direction is no longer present.

Normal shear above the wall at $y = 0.3$ cm did not provide any significant insight into the interaction process. On the other hand, the wall shear $\partial\langle U\rangle/\partial y$ at $y = 0$ was a good indicator of wall-eddy breakdown. The wall shears shown in figure 11(*c*) were computed from the vertical profile which was based on a spline-fit of the ensemble-averaged velocity. There was high wall shear under the high-speed streaks centred at $z \approx 8.8$ cm and $z \approx 10.2$ cm and low wall shear at the low-speed streak locations at $z \approx 9.5$ cm whenever an organized wall-eddy structure was present (i.e. for $1.1\pi \lesssim \phi \lesssim 2.4\pi$). This was consistent with the results of Swearingen & Blackwelder (1987). During breakdown (at $0.4\pi \leqslant \phi \lesssim 1.1\pi$), there was relatively high wall shear at *all* spanwise locations, indicative of a much fuller velocity profile.

Since the presence of the wall eddies provided large differences in the wall shear, the termination of this low- and high-wall-shear structure was used as the basis for a detection of the breakdown of the wall-eddy structure. In figure 11(*c*), the wall shear over the low-speed streak at $z \approx 9.5$ cm changes from low to high and back to low during a phase cycle. This trend is shown in figure 12 along with the corresponding shear under the high-speed region. The values shown in figure 12 are averaged over a

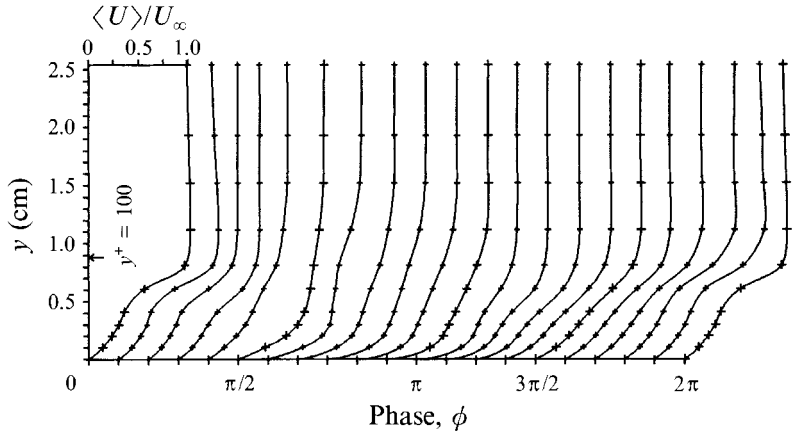

FIGURE 13. Ensemble-averaged velocity profiles for the 35% oscillation case at $x = 82.5$ cm, $z = 9.5$ cm. Twenty-one profiles at selected phase reference times of $\phi = 0, 0.1\pi, 0.2\pi, \ldots, 2\pi$ are shown. Note that the profile at $\phi = 2\pi$ is a repeat of the one at $\phi = 0$.

0.5 cm spanwise width centred about the low- or high-speed streak to eliminate the effect of small spanwise meandering. The difference between these two wall shears is shown in figure 12 by the solid line. The wall shear difference has a sharp decrease at $\phi \approx 0.4\pi$ and remains small during $0.8\pi \leqslant \phi \leqslant 1.1\pi$. This characteristic agreed well with the visual and hot-wire data and was used in the following to determine the breakdown phase.

5.3. *Details of the breakdown process*

Figure 13 shows the ensemble-averaged velocity profiles centred spanwise over a low-speed streak at $x = 82.5$ cm. Prior to the arrival of the accelerated fluid, the velocity profiles at $\phi < 0.4\pi$ are highly inflexional owing to the presence of the low-speed streak. By comparing the profiles at $\phi = 0.4\pi$ and 0.5π, it is apparent that the outer $-\omega_z$ eddy brings a large influx of relatively higher speed fluid. With the arrival of this accelerated fluid, the *ensemble-averaged* profiles at $\phi > 0.4\pi$ lose their inflexional shape and tend toward a much fuller shape consistent with the increased wall shear of figure 11(*c*). These fuller non-inflexional profiles occur during the breakdown phase, $0.4\pi \leqslant \phi \leqslant 1.1\pi$, due to the more intense mixing. For $\phi \gtrsim 1.1\pi$, inflexional velocity profiles with smaller wall shear reappear, indicating the presence of a low-speed streak. This entire process is repeated during subsequent phase cycles.

Since breakdown begins with the arrival of the accelerated fluid, the interesting interaction occurs sometime around $0.3\pi \lesssim \phi \lesssim 0.5\pi$. Two records of the instantaneous velocity profiles during this portion of the phase cycle are shown in figure 14. Prior to the arrival of the acceleration, the velocity profiles at $\phi \lesssim 0.35\pi$ were all highly inflexional as expected. However, the response of the flow when the outer high-speed fluid arrived was quite varied from one phase cycle to the next. In figure 14(*a*), the flow responded quite quickly with small-scale inflexional S-shaped profiles. During the next phase cycle in figure 14(*b*), the larger-scale inflexional S-shaped profiles were slightly delayed until $\phi \approx 2.45\pi$. This varied flow response to similar initial conditions and forcing ($-\omega_z$ eddy) is not unexpected for a transitional and/or turbulent flow and is reminiscent in many respects of the chaotic behaviour exhibited by some dynamical systems (cf. Aubry *et al.* 1988).

Conditional averaging can often obscure the strength and details of the flow events as the following example serves to illustrate. In figure 15(*a*), four instantaneous profiles

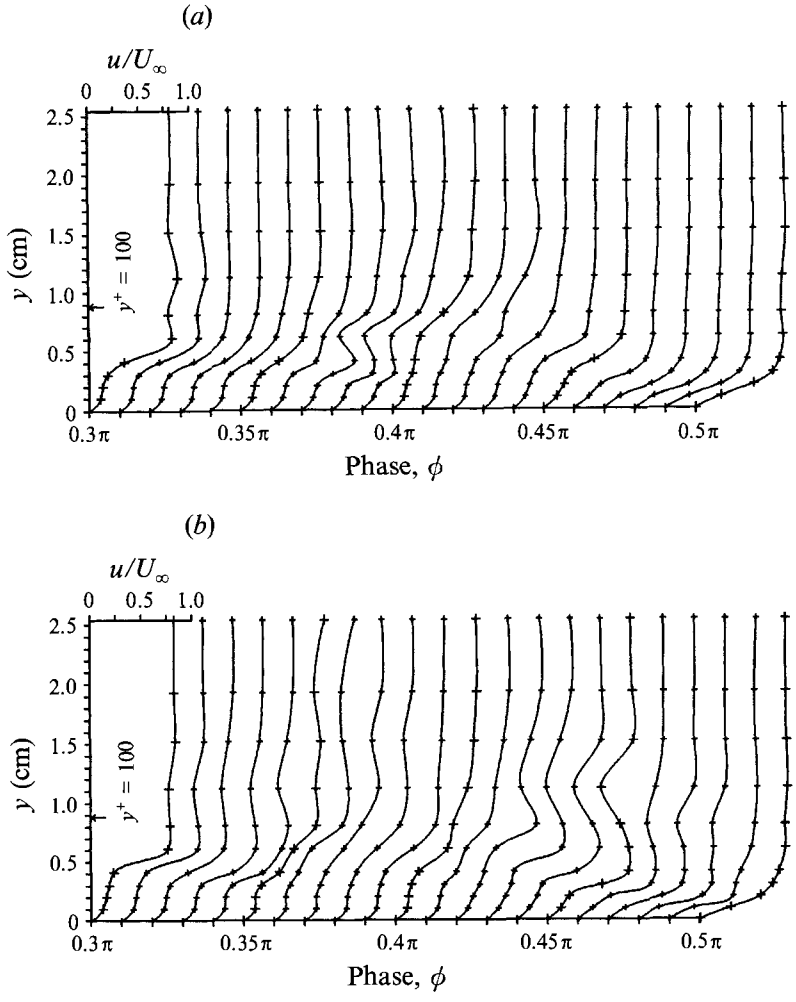

FIGURE 14. Instantaneous velocity profiles for the 35% oscillation case at $x = 82.5$ cm, $z = 9.5$ cm. (*a*) Part of the first cycle from figure 8. (*b*) Part of the second cycle from figure 8.

at $\phi = 0.3\pi$ are overlaid along with the appropriate ensemble-averaged profile from figure 13. Note that some instantaneous profiles are more inflexional than the ensemble average while others are less inflexional. More important, however, is that the height of the inflexion point varies from cycle to cycle. The standard ensemble average of these profiles produces an average profile with a much weaker inflexion. In figure 15(*b*), the four profiles of 15(*a*) are shifted vertically so that their inflexion points occur at the same elevation. It is easily seen that the 'standard' ensemble-averaged profile does not represent the typical shear intensity of the inflexional instantaneous profiles. With the 'standard' ensemble averaging, the maximum shear at the inflexion was $\partial\langle U\rangle/\partial y = 680\ \mathrm{s}^{-1}$. However when all 100 of the shifted instantaneous profiles were averaged, the solid-line profile in figure 15(*c*) resulted with a shear of $\partial\langle U\rangle/\partial y = 1030\ \mathrm{s}^{-1}$, i.e. a 50% increase. Also, the average height of the inflexion point moved from $y = 0.51$ cm for the 'standard' ensemble average to $y = 0.54$ cm for the 'shifted' ensemble average. By failing to account for an additional random independent variable which is important to the event being averaged (i.e. the height from the wall of the inflexion), the 'standard' ensemble average yielded a poorer representation of the true strength and

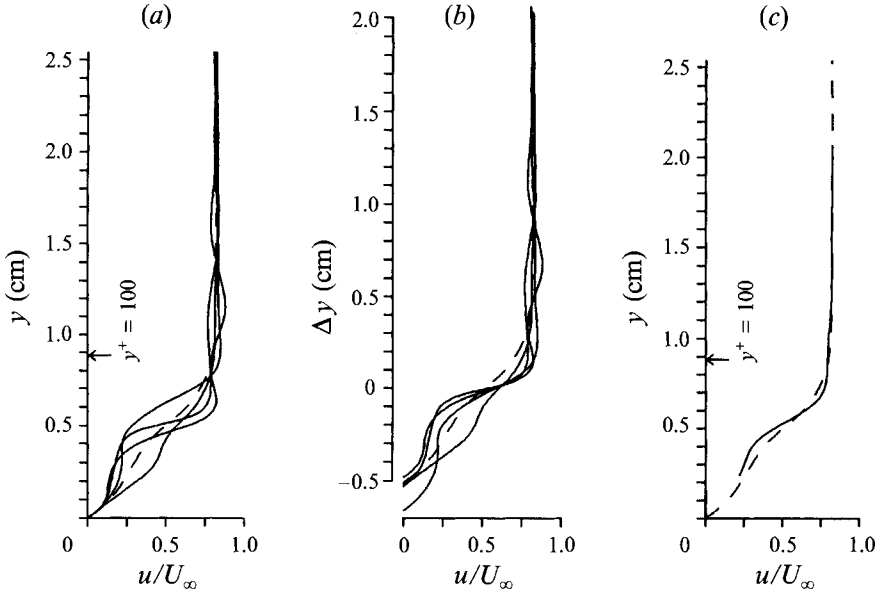

FIGURE 15. Velocity profiles for the 35% oscillation case at $x = 82.5$ cm, $z = 9.5$ cm, $\phi = 0.3\pi$. (*a*) Standard comparison: instantaneous (——) and ensemble-averaged (– – –) profiles; (*b*) profiles shifted to centre of inflexion point: instantaneous (——) and (standard) ensemble-averaged (– – –) profiles; (*c*) ensemble averaging about the centre of the inflection point (——) and standard ensemble averaging (– – –). Two of the instantaneous profiles in (*a*) and (*b*) are the first profiles shown in figure 14 ($\phi = 0.3\pi$).

character of the event. This serves as an important reminder that conditional averaging is highly dependent upon the condition and technique used.

6. Interaction with spanwise eddies of varying strength and sign

Results in §4.1 and figure 5 showed that the $-\omega_z$ eddy peak strength was increased as the airfoil oscillation pitch-down time was decreased. For the 25% oscillation case, the peak ω_z vorticity was -200 s^{-1} compared with a peak strength of -110 s^{-1} for the 35% case discussed in §5. Hence this important parameter was explored further.

6.1. *Flow visualization*

Flow visualization with the stronger $-\omega_z$ eddy, i.e. the 25% case, showed a stronger mixing of smoke particles, which indicated that breakdown appeared much more energetic than the 35% case. Since the visualized smoke patterns are a time-integrated effect, it appeared that breakdown was occurring over a longer time period (i.e. was initiated further upstream) for the stronger $-\omega_z$ case. On the other hand with the 50% case, i.e. a weaker $-\omega_z$ eddy, the wall eddy did not break down until further downstream. These results suggest that the stronger $-\omega_z$ outer eddies hasten the breakdown of wall eddies.

Flow visualization for the stationary airfoil case for the natural undisturbed Görtler case showed that all low-speed streaks were broken down by $x \approx 120$–125 cm. At this downstream location, low-speed streaks were also broken down during the entire phase cycle for the 25%, 35% and 50% cases. However it was possible to delay this breakdown beyond the naturally occurring case with the presence of a strong $+\omega_z$. This is illustrated in figure 16 with the 65% case which has a measured $+115$ s^{-1} peak-

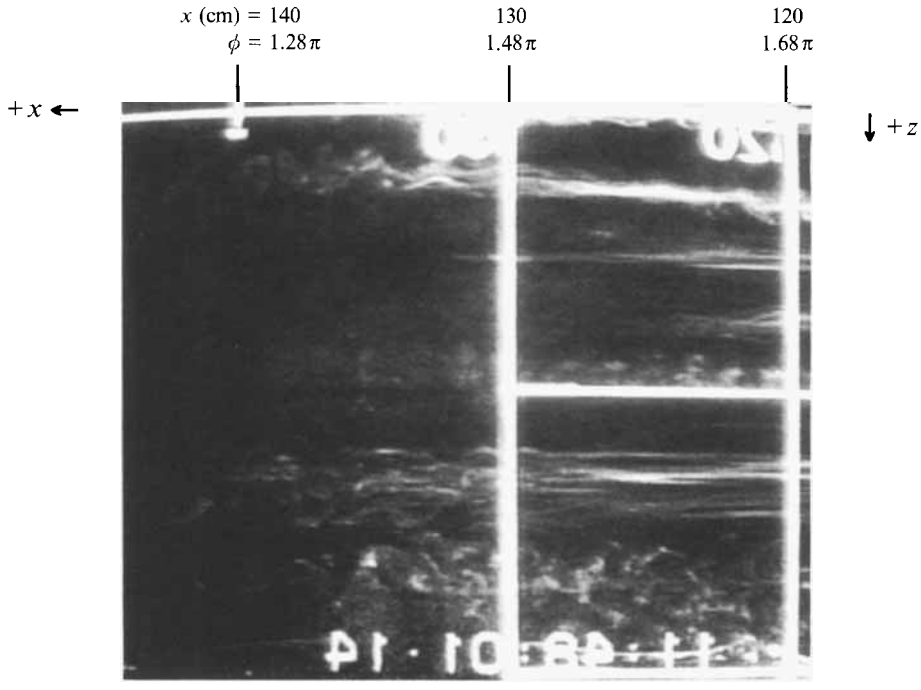

FIGURE 16. Flow visualization for 65% oscillation case.

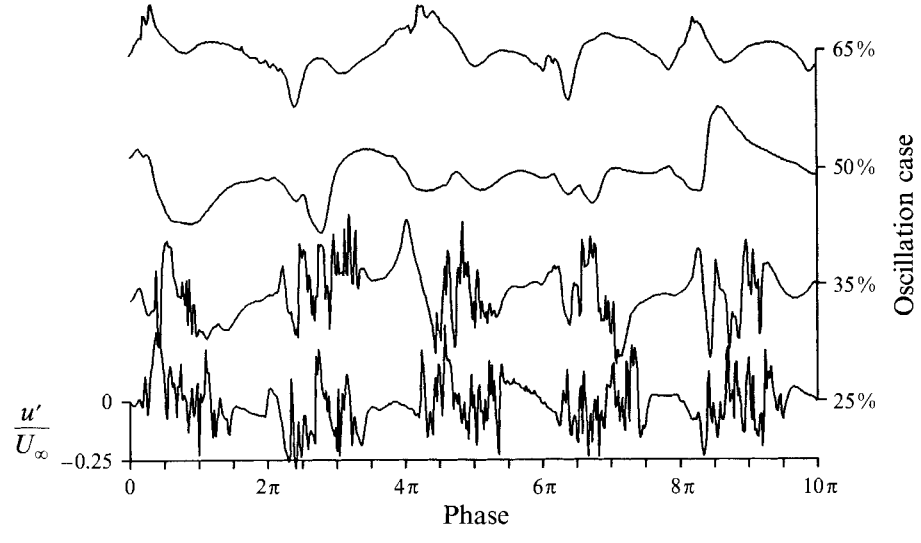

FIGURE 17. Instantaneous signal u'/U_∞ for various oscillation cases. Signal shown is at $x = 82.5$ cm, $y = 0.3$ cm and centred spanwise over a low-speed streak.

strength $+\omega_z$ eddy centred at about $\phi \approx 1.65\pi$. During the phase time associated with this strong $+\omega_z$ eddy, figure 16 shows distinct well-defined low-speed streaks. Thus, $+\omega_z$ outer eddies delay wall-eddy breakdown locally, and with a sufficiently strong $+\omega_z$ eddy, breakdown is delayed beyond the natural undisturbed breakdown location.

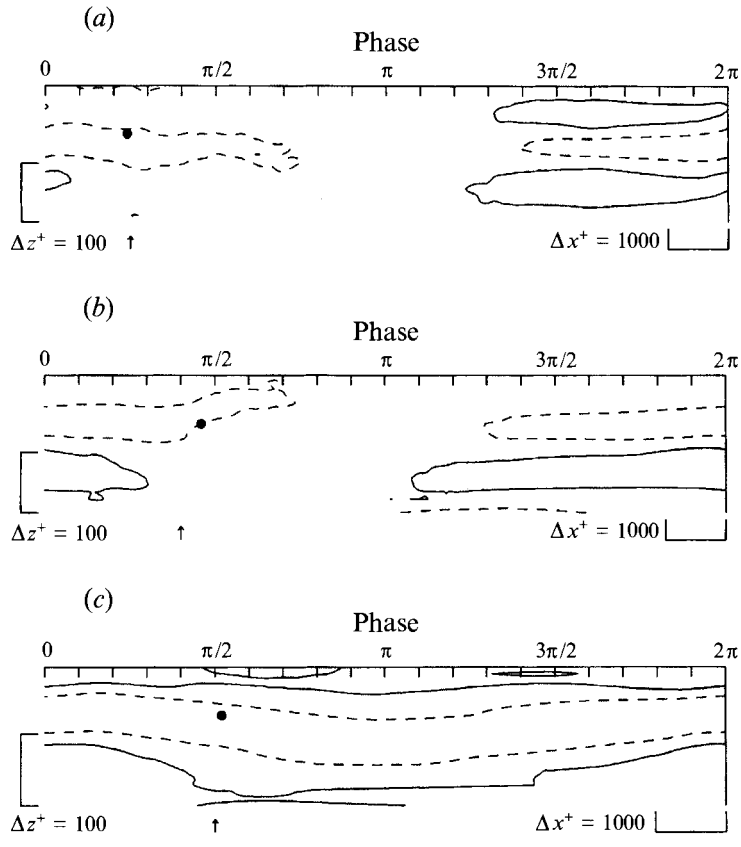

FIGURE 18. Iso-contours of $\langle U\rangle/U_\infty$ for various oscillation cases at $x = 82.5$ cm, $y = 0.3$ cm. ——, $\langle U\rangle - \bar{u} = -u'_{rms}$; ——, $\langle U\rangle - \bar{u} = +u'_{rms}$. $\bar{u}$ is the time-averaged velocity and u'_{rms} is the root-mean-square fluctuation from $\bar{u}$. ●, maximum u'_{sd} location; ↑, outer high-speed fluid arrival time. Note that x^+ increases from right to left and z^+ increases from top to bottom. Also note the order-of-magnitude difference in x^+ and z^+ scales. (*a*) 25% oscillation case, (*b*) 35% oscillation case, (*c*) 50% oscillation case.

6.2. *Velocity signals*

Figure 17 shows the instantaneous u'/U_∞ signal centred spanwise over a low-speed streak at $x = 82.5$ cm and $y = 0.3$ cm for the various oscillation cases. For the 25% oscillation case, there are high-frequency fluctuations corresponding to wall-eddy breakdown starting slightly before $\phi = 0.25\pi$. The characteristic flow behaviour for the 25% oscillation case is quite similar to the 35% case; however, a larger percentage of the phase cycle is broken down in the 25% case.

Approximately a third of each phase cycle has high-frequency fluctuations for the 35% case whereas it is closer to half for the very strong $-\omega_z$ eddies of the 25% case. The amplitude of the high-frequency fluctuations during breakdown are about the same [$u' \sim \pm 0.2U_\infty$] for both cases. High-frequency fluctuations were atypical for the 50% and 65% cases as shown in figure 17. Thus, wall eddies were generally not broken down at $x = 82.5$ cm for the moderate to weak $-\omega_z$ eddies. There were, however, fluctuations with low-frequency content (presumably low-speed streak meandering) correlated with the passage of a $-\omega_z$ eddy in the outer region. This was similar to the strong $-\omega_z$ eddy (35% case) further upstream such as the $x = 61$ cm signal of figure 9. Therefore, it appears that wall eddies respond more 'slowly' (in the sense that a

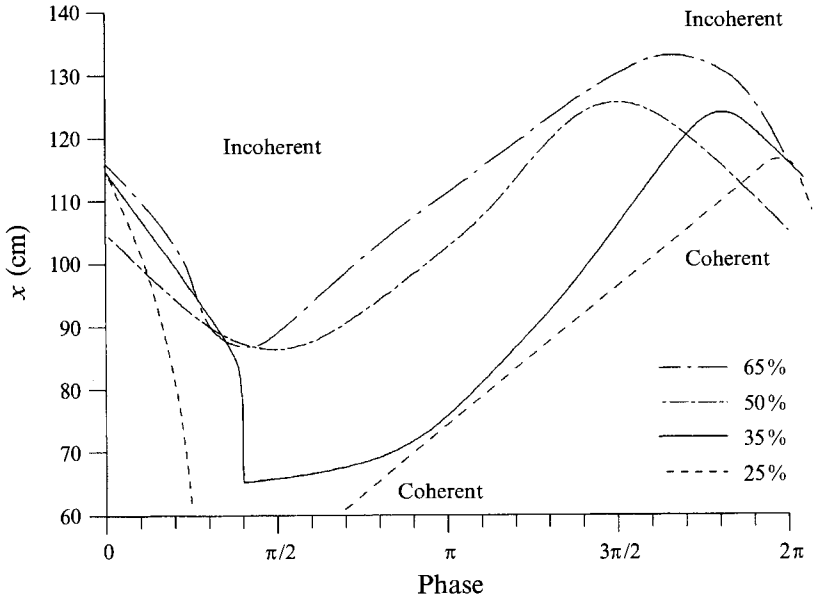

FIGURE 19. Loci of the breakdown locations for outer eddies of different strengths.

longer downstream distance is required before breakdown occurs) for the weak $-\omega_z$ outer eddies whereas the response is more 'rapid' for the very strong $-\omega_z$ eddies. Otherwise, the results show that the *character* of the breakdown process is quite similar to that presented in §5.

On the other hand, at 126 cm downstream, the instantaneous u' signals for the 65% oscillation case showed short durations when high-frequency fluctuations were absent. These quiescent periods occurred at about $\phi \approx 1.65\pi$ which is centred about the strong $+\omega_z$ eddy. Thus, the $+\omega_z$ eddies not only delayed the onset of the breakdown and transition, but they delayed the growth and completion of transition as well.

Figure 18 shows the ensemble-averaged results for the 25%, 35% and 50% oscillation cases at $x = 82.5$ cm and $y = 0.3$ cm. The low-speed streak is outlined by dashed contour lines and the acceleration arrival time is indicated with an arrow. The maximum standard deviation location is denoted by a solid circle although the particular u'_{sd} value is different in each case. The maximum standard deviation appears correlated with the arrival of the acceleration. For the 25% and 35% cases (see figures 18*a* and 18*b*), this indicates the commencement of breakdown. For the 50% case (see figure 18*c*), the wall eddy is not yet broken down so that correlation between maximum u'_{sd} and the arrival of the accelerated fluid suggests an intensification of low-speed streak meandering due to the presence of the outer structure. In this case, the increased oscillations are a precursor to breakdown further downstream. At $x = 104$ cm (Myose 1991), the maximum u'_{sd} and the arrival of the relatively higher-speed fluid were not correlated as well and the mixing associated with breakdown had shortened the low-speed streaks.

6.3. *Downstream development*

Figure 19 summarizes the breakdown loci in the (ϕ, x)-plane for the different outer eddies determined by the methods discussed in §5.2. Concentrating first on the 35% case, it is seen that at $x = 61$ cm, the wall eddies were not yet broken down. Quantitative measurements were taken at several downstream locations ($x = 61$, 72,

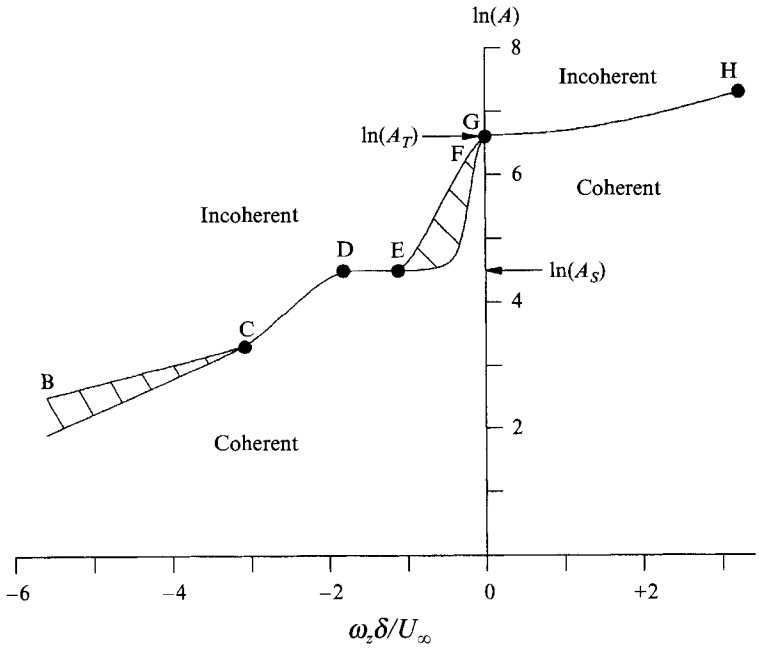

FIGURE 20. Effect of different strength eddies. Breakdown as a function of streamwise vortex net amplification factor A and non-dimensionalized outer-region structure strength $[\omega_z \delta / U_\infty]$. Shaded region signifies uncertainty in determining breakdown.

A_S = Görtler secondary instability location
A_T = Görtler transition to turbulence location
B = Very strong $-\omega_z$ eddy (e.g. from 25% case)
C = Strong $-\omega_z$ eddy (e.g. from 35% case)
D = Moderate strength $-\omega_z$ eddy (e.g. 50% case)
E = Weak $-\omega_z$ eddy (e.g. from 65% case)
F = High-free-stream turbulence level
G = Low-free-stream turbulence level
H = Strong $+\omega_z$ eddy (e.g. from 65% case).

82.5, 93, 104, 115 and 126 cm) and were supplemented by flow visualization. Extrapolating the results gave an initial breakdown at $x \approx 65$ cm. Breakdown temporally preceded the arrival of the acceleration for $x \gtrsim 85$ cm. With downstream distance, a larger percentage of the cycle was broken down, until the entire cycle was incoherent by $x \approx 125$ cm. Note that the furthest delay in breakdown occurs for phase times around $\phi \approx 1.8\pi$ corresponding to the presence of a $+\omega_z$ eddy in the outer region.

The breakdown loci for the outer eddies with different strengths was determined in a similar manner and is also shown in figure 19. At any given x-location, the figure shows that a larger percentage of the phase cycle is broken down as the $-\omega_z$ eddy is strengthened. Conversely, a larger percentage of the phase cycle remains coherent as the $+\omega_z$ eddy is strengthened. When the $+\omega_z$ eddy is *very* strong, i.e. the 65% case, wall-eddy breakdown is delayed beyond the natural Görtler transition location of $x \approx$ 120–125 cm. This is the x-location where wall eddies have developed sufficiently such that they transition to turbulence without any outside disturbance or influence. This stabilizing influence appears to be limited to phase times associated with the passage of $+\omega_z$ eddy.

Figure 19 shows that the arrival of the acceleration is associated with the initial

breakdown. That is, for the 25%, 35% and 50% oscillation cases, the leading edge of breakdown is correlated with the acceleration arrival times of $\phi \approx 0.25\pi$, 0.4π and 0.5π, respectively. For the 65% case, the primary $-\omega_z$ eddy is centred at about $\phi \approx 0.6\pi$ in figure 5. This compares with a breakdown leading edge of $\phi \approx 0.4\pi$ seen in figure 19, which is in reasonable agreement considering that breakdown phase times were determined primarily with flow visualization results for the 65% case. Figure 19 clearly shows that the location of the initial breakdown of the wall eddies moves upstream as the strength of the outer $-\omega_z$ eddy increases. Likewise, as the $+\omega_z$ eddy increases in strength, the transition process is delayed and the wall eddies break down further downstream.

Figure 20 summarizes the effects of changes in the outer eddy's strength and sign. The ordinate represents the strength or developmental state of the wall eddies and the abscissa provides the averaged peak ω_z strength. The streamwise vortex amplification factor A is given by (cf. Floryan & Saric 1984)

$$A = \exp \int_{x_N}^{x} \beta \, \mathrm{d}x,$$

where x_N is the streamwise location of the Görtler neutral stability and β is the growth rate of the Görtler vortices. Two notable points on the ordinate are the Görtler secondary instability point ($x \approx 85$ cm) denoted by A_S and the natural Görtler transition to turbulence point ($x \approx 120$ cm) denoted by A_T. When the $-\omega_z$ eddy is very strong, as in the 25% case (denoted by B), breakdown is initiated very far upstream where the wall eddies are at a very early stage of development. For a strong $-\omega_z$ eddy such as the 35% case (point C), breakdown is triggered upstream of the Görtler secondary instability point. Wall eddies at an advanced stage of development (i.e. $A \sim A_S$) are necessary to trigger breakdown by moderate strength and weak $-\omega_z$ eddies such as the 50% and 65% cases (denoted by D and E). Low-speed streak breakdown is hastened by high free-stream turbulence levels (point F) as demonstrated by Liepmann (1945) and Bippes (1978). At very low free-stream turbulence levels (point G), wall eddies do not break down until the natural transition point of A_T. Finally, wall eddies under the influence of strong $+\omega_z$ eddies such as the 65% case (denoted by H) remain coherent beyond the natural transition point of A_T.

7. Discussion

7.1. *Model of the interaction*

Breakdown may be summarized as the cessation of organized coherent structure together with the appearance of random motions. The cessation of organized structure was characterized by the termination of the low- and high-speed streaks, the deterministic spanwise shear and the wall shear structure. Random motions were manifested by intense mixing of smoke particles in the flow visualization, high-frequency fluctuations in the instantaneous signal and high levels of standard deviation. The leading edge of the breakdown was also indicated by the maximum peak level in the standard deviation. Breakdown phase times could be determined reasonably well by using the above events as criteria. The wall-shear-difference method described in § 5.2 was a more quantitative approach for determining the breakdown phase times and was used to supplement the above criteria. All methods gave breakdown phase times which generally agreed in spite of the fact that all of the methods use different aspects of the same phenomena.

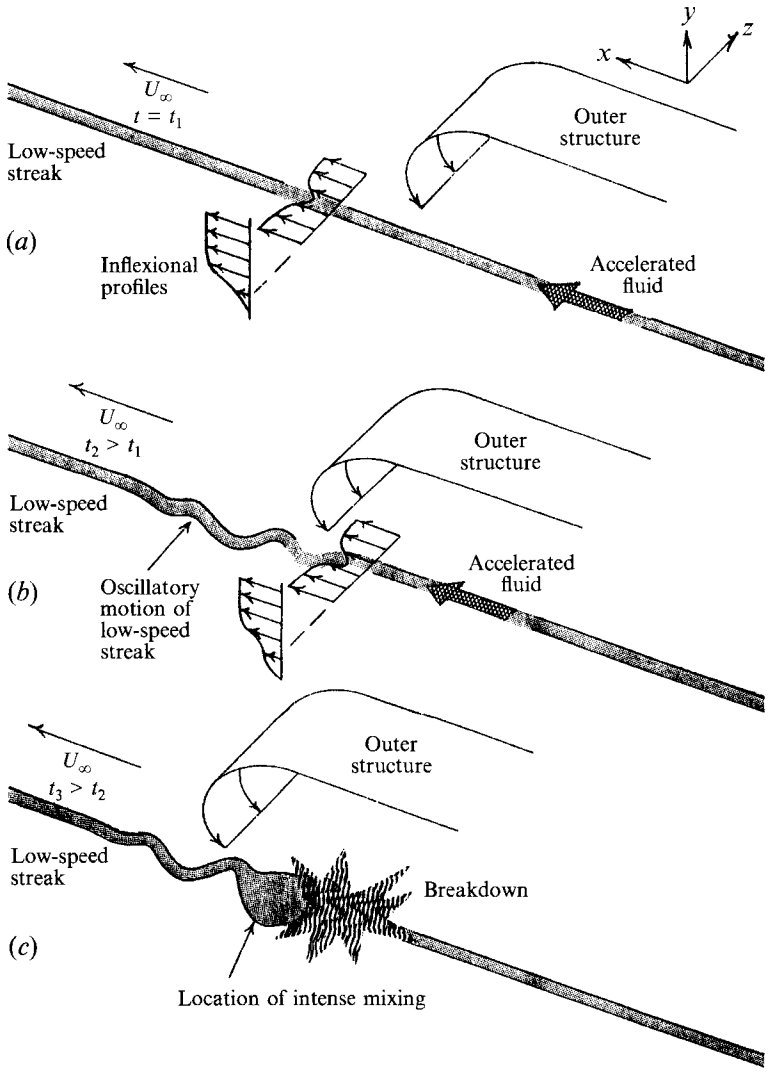

FIGURE 21. The breakdown process at three successive times.

Figure 21 summarizes the characteristic behaviour of the breakdown process at three progressive times. The low-speed streak structure appears initially with inflexional spanwise and normal profiles and is relatively undisturbed as the large outer structure appears upstream in figure 21 (*a*). As the outer eddy moves downstream in figure 21 (*b*), it encounters profiles with stronger inflexions because they have had more distance to develop. At some point downstream, the low-speed streaks begin an oscillatory motion possibly due to an inviscid instability associated with the inflexions. The $-\omega_z$ outer eddy and the accelerated region are moving at a faster velocity and encroach upon the oscillation. The wall-eddy oscillation appears to intensify, possibly due to this encroachment or due to the nonlinear growth or other mechanisms. Breakdown is subsequently triggered in fixture 21 (*c*) as the acceleration region arrives and violent mixing occurs. The mixing involves high-frequency random motions and is most intense around the maximum velocity deficit location. As the outer structure proceeds downstream, the spatial extent of the random motions grows as indicated in figure 19.

7.2. *Comparison with turbulent wall layers*

Flow visualization of the breakdown process in the present experiment is quite similar to the turbulent-boundary-layer bursting process described by Kline *et al.* (1967) and others. Some of the details of this breakdown process were illustrated earlier in figure 13 with ensemble-averaged velocity profiles. Preceding breakdown, the velocity profiles were inflexional owing to the presence of the low-speed streak. The leading edge of breakdown was indicated by the maximum standard deviation. Upon breakdown, the ensemble-averaged velocity profiles became 'fuller' in shape. In actual turbulent boundary layers Blackwelder & Kaplan (1976), using the VITA detection technique, found a similar behaviour of inflexional profiles preceding the burst and 'full' profiles following the burst. Blackwelder & Swearingen (1989) have shown that the spanwise inflexional profiles exist on the sides of the low-speed streaks in both flows.

In the natural undisturbed Görtler flow case, Swearingen & Blackwelder (1987) showed that the transition location was strongly localized in the spanwise location; i.e. it was dependent upon the particular low-speed streak chosen. In the present case, the flow visualization in figure 7 showed that breakdown was uniform in the spanwise direction. That is, the leading edge of breakdown was correlated with the arrival of the accelerated fluid and was not a strong function of the particular low-speed streak chosen. This supports the idea that the $-\omega_z$ *outer eddies do interact with the near-wall eddies, affecting their breakdown.* Similar ideas have been proposed by Brown & Thomas (1977), Chen & Blackwelder (1978) and others in the turbulent case. These results suggest that the dynamical characteristics exhibited in this emulation experiment are quite similar to those of actual moderate-Reynolds-number flat-plate turbulent boundary layers.

In another point of comparison, McLean (1990) presented instantaneous results from a flat-plate turbulent boundary layer in an orientation similar to figure 18. He found low-speed streaks of varying lengths terminated by VITA detection signals. Relatively long-duration low-speed streaks were terminated by a strong insweep of high-speed fluid, i.e. an acceleration, comparable to the situation shown in figures 18(*a*) and 18(*b*). On the other hand, McLean found that relatively short-duration, low-speed streaks were terminated *without* a strong insweep. Myose (1991) found a comparable situation in the present study at $x = 104$ cm where the low-speed streaks were in a terminal stage. This suggests that VITA-detected 'burst' events which involve short low-speed streaks may possibly be 'old' decaying bursts.

7.3. *Drag reduction implications*

Weaker $-\omega_z$ eddies trigger breakdown only if the wall eddies are sufficiently well developed (see case E in figure 20). Conversely, very strong $-\omega_z$ eddies can trigger breakdown of less-developed wall eddies (see case B in figure 20). This suggests that reducing the growth of the wall eddies *or* the outer eddies may result in less mixing and possibly drag reduction. In a study of three-dimensional outer eddies, Myose (1991) found the spatial position of the wall eddies relative to the spanwise centre of a three-dimensional outer-region structure affects the phase location of the breakdown. Thus, whether a wall eddy is broken down or not is dependent on a combination at least three factors:

(i) the stage of development of the wall eddy;
(ii) the strength of the outer-region eddy;
(iii) the spanwise offset between the wall and outer-region eddies in the case of three-dimensional outer eddies.

In actual turbulent boundary layers, there are wall eddies at different stages of development, outer-region structures with varying $-\omega_z$ strengths, and different spatial offsets between the two structures. Therefore, countless combinations of these and possibly other different factors make the turbulent-boundary-layer bursting process an extremely complicated and random affair.

Swearingen & Blackwelder (1987) showed that low-speed streaks can break down autonomously if left undisturbed. However, wall-eddy breakdown is hastened by the presence of $-\omega_z$ eddies according to the present experiment. Since there is a relationship between pressure and the vortices, the passage of an outer $-\omega_z$ eddy is akin to a transient pressure gradient. Therefore, the results of the present experiment are consistent with the numerical modelling study of Aubry *et al.* (1988) where burst-like events could be generated autonomously in the wall region, but were more readily triggered by pressure fluctuations from the outer part of the boundary layer.

Stronger $-\omega_z$ eddies were found to break down wall eddies more easily in figure 20. Thus, stronger outer-region eddies have a larger influence upon the bursting process. This was consistent with the results of McLean (1990) where 'inactive' outer-region scales grew in size and strength as $Re \rightarrow \infty$. Similar results have been reported by Naguib & Wark (1992). This suggests that the outer region may have a stronger influence upon the bursting process as the Reynolds number is increased.

One drag-reducing apparatus employed in the outer region is the large eddy break-up (LEBU) device. Chang & Blackwelder (1990) suggested that LEBUs affect primarily the outer region by decreasing the entrainment and boundary-layer growth which in turn reduces drag. The LEBUs may also inhibit the violet interaction between the outer high-speed fluid and the low-speed streak. Dowling (1985) found that LEBUs shed concentrated positive vorticity [$+\omega_z$ eddy] in their wakes which acts to cancel the destabilizing influence of the $-\omega_z$ eddy. Such shedding of a $+\omega_z$ eddy by the LEBU could lead to drag reduction according to the present experiment.

8. Summary

A moderate-Reynolds-number turbulent boundary layer was emulated experimentally and the resulting interaction of eddy structures was studied. Streamwise vortices in the presence of strong wall shear developed low-speed streaks and inflexional velocity profiles. Then, spanwise meandering of the low-speed streak and low-frequency velocity fluctuations ensued. Wall-eddy breakdown was subsequently triggered with the arrival of high-speed fluid associated with the outer region. The breakdown *process* involved wall-eddy development, oscillation and breakdown triggered by the outer high-speed fluid. The breakdown *itself* involved the cessation of organized coherent structure and the appearance of random incoherent motions in the near-wall region. The low-speed streak was broken down as a result of an acceleration associated with the outer structure, and the ensuing mixing caused high-frequency random motions. This violent mixing was most energetic at the maximum velocity deficit of the inflexional velocity profile. With downstream distance, the incoherent portion encompassed a larger fraction of the phase cycle until the entire flow was eventually broken down.

At far downstream locations, the leading edge of breakdown preceded the arrival of outer high-speed fluid. This suggests that turbulent-boundary-layer 'burst' events involving short-duration low-speed streaks, terminated *without* a strong insweep of high-speed fluid, may possibly be 'old' bursts. In this case, the initial breakdown was

triggered by an insweep far upstream of the measuring location and the remaining low-speed streak is decaying and in its terminal stage of existence.

Although wall eddies can break down autonomously, the presence of and interaction with outer-region $-\omega_z$ eddies hastened their breakdown. Increasing the $-\omega_z$ eddy strength resulted in further hastening of the breakdown. Conversely, $+\omega_z$ eddies were found to delay wall-eddy breakdown locally, with further delays resulting from stronger $+\omega_z$ eddies. This suggests that the outer region plays a significant role in the turbulent-boundary-layer bursting process.

Because the present results were obtained at a single Reynolds number, they do not help clarify the scaling of the bursting frequency. Although the conclusion is that eddies in the outer region can and do alter the wall layer of the model, the fully turbulent wall region is a much more complicated region. For example, the turbulent region has a continuum of eddy scales whereas the emulated flow has primarily two scales. In the turbulent case, it seems that the interaction with the outer region produces a strong normal component in the near-wall region and that was not effectively modelled by the emulation. In particular Falco (1990) has shown that the outer region of the turbulent flow has smaller-scale eddies and pockets associated with it and these may be the mode of communication between the two regions. An alternative point of view is that the ω_x eddies in the model were allowed to develop in an isolated environment without being subjected to the random perturbations of the turbulence due to the outer region.

The authors acknowledge the assistance of Dennis Plocher for the computer interfacing of electro-mechanical devices. We also thank the reviewers for their suggestions for clarifications. This work was sponsored by the Office of Naval Research under contract N00014-89-J-1400 and the Air Force Office of Scientific Research under contract F49620-85-C-0080. Their generous support is greatly appreciated.

REFERENCES

ACARLAR, M. S. & SMITH, C. R. 1987 *J. Fluid Mech.* **175**, 1.

AIHARA, Y. & KOYAMA, H. 1981 *Trans. Japan Soc. Aero. Space Sci.* **24**, 78

AUBRY, N., HOLMES, P., LUMLEY, J. L. & STONE, E. 1988 *J. Fluid Mech.* **192**, 115.

BIPPES, H. 1978 *NASA TM* 75243.

BLACKWELDER, R. F. 1983 *Phys. Fluids* **26**, 2807.

BLACKWELDER, R. F. & KAPLAN, R. E. 1976 *J. Fluid Mech.* **76**, 89.

BLACKWELDER, R. F. & KOVASZNAY, L. S. 1972 *Phys. Fluids* **15**, 1545.

BLACKWELDER, R. F. & SWEARINGEN, J. D. 1989 *Near wall turbulence, Proc. Zaric Mem. Conf., 1988*, p. 268. Hemisphere.

BROWN, G. L. & THOMAS, A. S. W. 1977 *Phys. Fluids* **20**, S243.

CANTWELL, B. J. 1981 *Ann. Rev. Fluid Mech.* **13**, 457.

CHANG, S.-I. & BLACKWELDER, R. F. 1990 *J. Fluid Mech.* **213**, 419.

CHEN, C. & BLACKWELDER, R. F. 1978 *J. Fluid Mech.* **89**, 1.

CORINO, E. R. & BRODKEY, R. S. 1969 *J. Fluid Mech.* **39**, 1.

DOWLING, A. P. 1985 *J. Fluid Mech.* **160**, 447.

FALCO, R. E. 1980 *AIAA* 80-1356.

FALCO, R. E. 1990 *Phil. Trans. R. Soc. Lond.* A **336**, 103.

FLORYAN, J. M. & SARIC, W. S. 1984 *AIAA J.* **22**, 1529.

GÖRTLER, H. 1940 *Math. Phys. Klasse* **2**, 1 (also *NACA TM* 1375).

GUEZENNEC, Y., PIOMELLI, U. & KIM, J. 1989 *Phys. Fluids* A **1**, 764.

ITO, A. 1985 *Trans. Japan Soc. Aero. Space Sci.* **33**, 166.

JAYARAMAN, R., PARIKH, P. & REYNOLDS, W. C. 1982 *Rep.* TF-18, Stanford University.

KIM, H. T., KLINE, S. J. & REYNOLDS, W. 1971 *J. Fluid Mech.* **50**, 133.

KLEBANOFF, P. S. 1954 *NACA TN* 3178.

KLINE, S. J., REYNOLDS, W. C., SCHRAUB, F. A. & RUNSTADLER, P. W. 1967 *J. Fluid Mech.* **30**, 741.

KLINE, S. J. & ROBINSON, S. K. 1989 *Near wall turbulence, Proc. Zaric Mem. Conf., 1988,* p. 200. Hemisphere.

KOOCHESFAHANI, M. M. 1989 *AIAA J.* **27**, 1200.

LIEPMANN, H. 1945 *NACA WR* 4J28.

MCLEAN, I. R. 1990 The near wall eddy structure in an equilibrium turbulent boundary layer. PhD dissertation, University of Southern California.

MYOSE, R. Y. 1991 An experimental emulation of the interaction of turbulent boundary layer eddy structures. PhD dissertation, University of Southern California.

MYOSE, R. Y. & BLACKWELDER, R. F. 1991 *AIAA J.* **29**, 1901.

NAGUIB, A. M. & WARK, C. E. 1992 *J. Fluid Mech.* **243**, 541.

ROBINSON, S. K. 1991 *Ann. Rev. Fluid Mech.* **23**, 601.

SMITH, C. R. 1978 In *Coherent Structures of Turbulent Boundary Layers* (ed. C. R. Smith & D. E. Abbott), p. 48. Lehigh University.

SWEARINGEN, J. D. 1985 *The growth and breakdown of streamwise vortices in the presence of a wall.* PhD dissertation, University of Southern California.

SWEARINGEN, J. D. & BLACKWELDER, R. F. 1987 *J. Fluid Mech.* **182**, 225.

TALMON, A. M., KUNEN, J. M. G. & OOMS, G. 1986 *J. Fluid Mech.* **163**, 459.